Sparse and Scalable Eigenstrain-based Reduced Order Homogenization Models for Polycrystal Plasticity

Xiang Zhang and Caglar Oskay*

Department of Civil and Environmental Engineering
Vanderbilt University
Nashville, TN 37235

Abstract

In this manuscript, accelerated, sparse and scalable eigenstrain-based reduced order homogenization models have been developed for computationally efficient multiscale analysis of polycrystalline materials. The proposed model is based on the eigenstrain-based reduced order homogenization (EHM) approach, and provides significant efficiency in analysis of structures composed of complex polycrystalline microstructures. The acceleration is achieved by introducing sparsity into the linearized reduced order system through selectively considering the interactions between grains based on the idea of grain clustering. The proposed approach results in a hierarchy of reduced models that recovers eigenstrain-based homogenization, when full range of interactions are considered, and degrades to the Taylor model, when all inter-grain interactions are neglected. The resulting sparse system is solved efficiently using both direct and iterative sparse solvers, both of which show significant efficiency improvements compared to the full EHM. A layer-by-layer neighbor grain clustering scheme is proposed and implemented to define ranges of grain interactions. Performance of the proposed approach is evaluated by comparing the results against the full EHM and crystal plasticity finite element (CPFE) simulations.

Keywords: Sparse; Scalable; Reduced order model; Grain cluster; Multiscale model; Polycrystal plasticity.

1 Introduction

We are concerned with the development of a concurrent multiscaling strategy for polycrystalline materials that couples the mechanical behavior at the scale of grains to that of the

*Corresponding author address: VU Station B#351831, 2301 Vanderbilt Place, Nashville, TN 37235. Email: caglar.oskay@vanderbilt.edu

overall structure or a structural component. This development is particularly critical in the prediction of localized phenomena (e.g., damage initiation in a structural component), which are affected by the local microstructure morphology. It also poses significant challenges in two respects. The first challenge is the tremendous memory and computational costs associated with the evaluation of complex polycrystalline morphologies, especially in the context of a multiscale analysis. The second challenge is the development of constitutive models that accurately capture the relevant physical phenomena that lead to damage initiation within the material microstructures. This manuscript addresses the former challenge.

Crystal plasticity finite element (CPFE) method directly resolves all microstructural heterogeneities using finite element discretization, and employs the crystal plasticity theory-based evolution equations to describe the microstructural behavior. CPFE fully considers all interactions between the grains, ensure compatibility and equilibrium, and hence captures the local response accurately provided that the evolution equations accurately capture the underling physical mechanisms. CPFE is a very powerful and versatile tool that has been employed to solve crystal plasticity problems under various loading conditions across different deformation mechanisms (for a comprehensive review, see Ref. [45]). However, high computational cost of CPFE simulations on a polycrystalline representative volume element (RVE) makes its use in concurrent multiscale modeling frameworks (e.g., computational homogenization [49, 36, 17, 26]) for structural scale analysis impractical, even on today's high performance hardware. Reduced order representation of the microstructural behavior is therefore essential for structural scale analysis that takes into account the grain level behavior.

Sachs [47] and Taylor [51] models can be viewed as among the earliest attempts of polycrystal plasticity homogenization. Both models disregard grain shapes and interactions, and further assume either iso-stress or iso-strain condition for the grains, which violate compatibility or equilibrium, respectively. In the context of Taylor model, the spectral crystal plasticity method developed by Knezevic et al. [24] constructs spectral representation of the crystal plasticity constitutive relationship a priori, and retrieves local spectral interpolation using the fast Fourier transformation (FFT) during any specific simulation later on. This approach has been recently embedded into finite element framework and implemented on high performance computer hardware [37, 23].

The grain cluster method [19, 20, 53] relaxes the excessive constraints imposed by the Taylor model by applying the macroscale deformation gradient onto a cluster of grains, thereby accounting for interactions between neighboring grains. The grain cluster approach typically restricts grain morphologies to regular geometries, and the elimination of this restriction is an ongoing research topic [55]. Viscoplastic self-consistent (VPSC) formulation [3, 29] approximates each grain as an ellipsoidal inclusion embedded in a homogeneous equivalent media representing the homogenized behavior of the polycrystal. Among significant extensions of the VPSC model are the inclusion of finite strain elasto–viscoplastic effects [54], embedding into finite element framework [48, 25], and extensions to better account for grain interactions [28, 50]. Despite significant progress, the ellipsoidal representation of the grain morphologies limits ac-

curacy of grain interactions.

The FFT method pioneered by Suquet and coworkers [38, 35] applied to the crystal plasticity problem [27, 30, 16] solves the system using the FFT on regular grids that are often obtained from the voxelized microstructure images. FFT considers full grain interactions and provides high efficiency compared with CPFE. Michel and Suquet extended their non-uniform transformation method [33, 34] into the modeling of polycrystalline materials and reported two orders of magnitude speedup compared with full field simulation using FFT [32]. While the FFT method has seen significant success, employing less restrictive boundary conditions and loss of accuracy due to the use of regular grids remain open questions.

More recently, the eigendeformation-based reduced order homogenization (EHM) [39] has been extended to polycrystal plasticity [60]. EHM is based on the transformation field theory [14, 15] and operates in the context of computational homogenization. EHM pre-computes certain microstructure information (i.e., concentration tensors, interaction tensors) and approximates the microscale problem using a much smaller basis by prescribing spatial variation of inelastic response fields over the microstructure. A significant benefit of the EHM approach is that it numerically approximates the influence functions using actual grain morphologies. Depending on order reduction strategy used, EHM can provide either sub-grain level or grain-level resolution [60]. While the EHM approach has been shown to provide two orders of magnitude computational efficiency compared to CPFE simulations, we demonstrate in this manuscript that the efficiency characteristics of EHM degrades as larger microstructures are considered.

The application of eigenstrain concepts to heterogeneous materials that exhibit path- and history-dependent response dates back to Dvorak and coworkers, who studied failure in fiber reinforced composites using the transformation field analysis ([14, 15]). Oskay and coworkers employed the EHM approach to investigate the nonlinear response of heterogeneous materials [39, 56, 12, 22, 8, 61, 59] including polycrystalline plasticity, viscoplasticity and damage mechanics under a range of loading and environmental conditions. Suquet and coworkers employed non-uniform transformation field analysis to study similar problems using path- and history-dependent material models to describe the behavior of composite constituents and polycrystal plasticity [33, 34, 32].

This manuscript presents accelerated, sparse and scalable eigenstrain-based reduced order homogenization models for computationally efficient multiscale analysis of polycrystalline materials. The proposed models are based on the EHM approach, and provide significant efficiency in analysis of structures composed of complex polycrystalline microstructures. The grain-cluster concept is used to identify a neighborhood for each grain, within which the interactions (i.e., short-range interactions) are considered, whereas the interactions with grains outside the neighborhood (i.e., long-range interactions) are neglected. Computationally, this strategy introduces sparsity into the linearized reduced order system, facilitating the use of sparse solvers. This manuscript presents the following novel contributions: (1) A sparse EHM approach has been formulated and a new set of concentration tensors and interaction tensors

are derived by only considering interactions between each grain and a cluster of predefined neighboring grains, and enforcing the constraints derived from transformation field analysis; (2) A consistent grain-clustering scheme is proposed to identify the grain cluster for each grain. We provide a thorough assessment of the performance of the sparse EHM formulation for a range of microstructure sizes using direct and iterative sparse solvers.

The remainder of this manuscript is organized as follows: Section 2 provides a brief overview of the formulation of eigenstrain-based reduced order homogenization for polycrystal plasticity, and the assessment of its computational efficiency compared with CPFE as a function of microstructure size. The sparse EHM system is formulated in Section 3 by considering interactions between each grain and a cluster of selected grains. In Section 4, a consistent grain-clustering scheme for identifying neighboring grain-clusters is proposed. Appropriate linear solvers are identified and implemented for maximum computational efficiency. Section 5 evaluates the performance of the sparse EHM by comparing the results with the full EHM and CPFE. Conclusions and future work are discussed in Section 6.

2 EHM for polycrystal plasticity

This section summarizes the reduced multiscale system that results from the eigenstrain-based polycrystal plasticity modeling approach recently proposed by the authors [60]. A brief overview is provided herein, since the proposed formulation builds on the EHM approach. The reduced order model starts from a two-scale analysis of the governing equation, which results in the classical form of coupled nonlinear microscale equation (defined over the representative volume) and the homogenized macroscale problem (defined over the structural domain).

Consider a macroscopic body Ω, with a locally periodic polycrystalline microstructure domain Θ in a two-scale problem setting as shown in Fig. 1. The ratio (ζ) between the characteristic lengths of the macrostructure, parameterized by $\mathbf{x}$, and the microstructure, parameterized by $\mathbf{y}$, is assumed to be small (i.e., $0 < \zeta \ll 1$). The current formulation considers small deformation assumption at the microscale, where microstructure undergoes inelastic deformations due to dislocation slip without texture evolution. The governing equation of the macroscale boundary value problem associated with the heterogeneous body is obtained as ([39, 60]):

$$\nabla \bar{\boldsymbol{\sigma}}(\mathbf{x}, t) + \bar{\mathbf{b}}(\mathbf{x}, t) = 0 \qquad \mathbf{x} \in \Omega \tag{1}$$

in which, $\bar{\boldsymbol{\sigma}}$ is the macroscopic Cauchy stress tensor, $\bar{\mathbf{b}}$ the body force, and ∇ denotes the gradient operator. The boundary conditions are given as:

$$\bar{\mathbf{u}}(\mathbf{x}, t) = \bar{\mathbf{u}}_0 \qquad \mathbf{x} \in \Gamma^u \tag{2}$$

$$\mathbf{n} \cdot \bar{\boldsymbol{\sigma}}(\mathbf{x}, t) = \bar{\mathbf{t}}_0 \qquad \mathbf{x} \in \Gamma^t \tag{3}$$

in which, $\bar{\mathbf{u}}$ denotes the macroscopic displacement field, $\bar{\mathbf{u}}_0$ and $\bar{\mathbf{t}}_0$ are the prescribed displace-

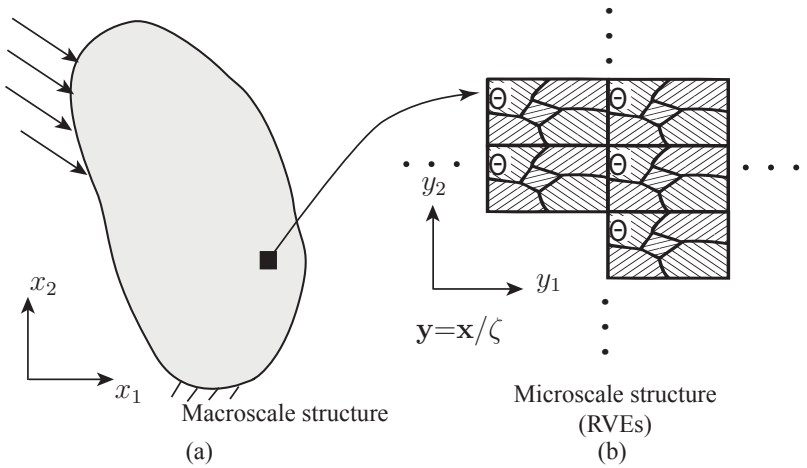

Figure 1: Macroscale and microscale structure in a two-scale problem setting.

ment and traction on the boundaries Γ^u and Γ^t, where $\Gamma^u \cup \Gamma^t = \partial\Omega$ and $\Gamma^u \cap \Gamma^t = \emptyset$. $\mathbf{n}$ is the unit normal to Γ^t. Macroscale strain tensor, $\bar{\boldsymbol{\epsilon}}(\mathbf{x}, t)$ is expressed in terms of macroscale displacement based on small deformation assumption:

$$\bar{\boldsymbol{\epsilon}} = \nabla^s \bar{\mathbf{u}}(\mathbf{x}, t) \tag{4}$$

where ∇^s is the symmetric gradient operator.

Equations (1)-(4) define the macroscale problem, whereas the eigenstrain-based reduced order homogenization model is used to approximate the microscale problem. Model order reduction is achieved by first expressing the microscale component of the displacement field in terms of "influence functions", which define its variation over the microstructure. The influence functions are numerical Green's functions computed by solving linear-elastic problems defined over the RVE. The influence functions are computed prior to macroscale analysis since they depend only on elastic properties of the constituents and the microstructure geometry. The inelastic strain fields within a microstructure (or eigenstrains in the context of transformation field theory [14, 15]) are approximated by a coarse discretization. Similar to finite elements, the discretization (i.e., each coefficient) is associated with a subdomain (part) of the microstructure domain. Employing the microscale displacement discretization and the eigenstrain approximation, the microscale governing equations are converted to an algebraic system, which is solved for the small set of eigenstrain coefficients. The constitutive equation at the microscale is expressed as:

$$M^{(\beta)}_{ijkl}\dot{\sigma}^{(\beta)}_{kl}(\mathbf{x}, t) - \sum_{\alpha=1}^{n} \left[P^{(\beta\alpha)}_{ijkl} - \delta^{(\alpha\beta)} I_{ijkl}\right] \dot{\mu}^{(\alpha)}_{kl}(\mathbf{x}, t) = A^{(\beta)}_{ijkl}\dot{\bar{\varepsilon}}_{kl}(\mathbf{x}, t) \tag{5}$$

where, $\boldsymbol{\sigma}^{(\beta)}$ denotes Cauchy stress of part β, $\boldsymbol{\mu}^{(\alpha)}$ the inelastic strain in part α, $\dot{f}$ indicates time derivative of f (i.e., $\dot{f} = \frac{\mathrm{d}f}{\mathrm{d}t}$), $\boldsymbol{\delta}$ is the Kronecker delta function, $\mathbf{I}$ the fourth order identity tensor (i.e., $I_{ijkl} = (\delta_{ik}\delta_{jl} + \delta_{il}\delta_{jk})/2$). $\mathbf{M}^{(\beta)}$ is the compliance tensor, $\mathbf{P}^{(\beta\alpha)}$ and $\mathbf{A}^{(\beta)}$

the interaction and concentration tensors calculated from the elastic and inelastic influence functions (see the Appendix for more details). Macroscale stress is then computed as the volume average of the part-average stress coefficients:

$$\bar{\sigma}_{ij} = \sum_{\beta=1}^{n} \frac{|\Theta^{(\beta)}|}{|\Theta|} \sigma_{ij}^{(\beta)} \tag{6}$$

in which, $|\Theta^{(\beta)}|$ denotes the volume of part β and $|\Theta|$ is the volume of the microstructure.

Due to the static texture and dislocation slip being the sole source of plastic deformation, inelastic strain in part α, $\boldsymbol{\mu}^{(\alpha)}$, results from dislocation slip over all slip systems:

$$\dot{\mu}_{ij}^{(\alpha)}(\mathbf{x}, t) = \sum_{s=1}^{N} \dot{\gamma}^{s(\alpha)}(\mathbf{x}, t)\, Z_{ij}^{s(\alpha)} \tag{7}$$

in which, $\mathbf{Z}^{s(\alpha)}$ is the Schmid tensor of slip system s in part α, uniquely describing the orientation of the s^{th} slip system as the dyadic product of the slip direction, $\mathbf{n}^{s(\alpha)}$, and the normal to the slip plane $\mathbf{m}^{s(\alpha)}$, (i.e., $Z_{ij}^{s(\alpha)} = n_i^{s(\alpha)} m_j^{s(\alpha)}$). EHM admits arbitrary form for the flow rule describing the shear strain rate $\dot{\gamma}^{s(\alpha)}$ as well as the hardening rules defined over part-averaged quantities. A flow rule frequently used for face-centered cubic (FCC) crystals is employed in this study ([44, 41]):

$$\dot{\gamma}^{s(\alpha)}(\mathbf{x}, t) = \dot{\gamma}_0 \left(\frac{\left|\tau^{s(\alpha)}(\mathbf{x}, t)\right|}{g^{s(\alpha)}(\mathbf{x}, t)} \right)^{1/m} \operatorname{sgn}\left(\tau^{s(\alpha)}(\mathbf{x}, t)\right) \tag{8}$$

where, $\dot{\gamma_0}$ is the reference shear strain rate, m the rate sensitivity parameter and $\tau^{s(\alpha)}$ resolved shear stress on slip system of part α (i.e., $\tau^{s(\alpha)}(\mathbf{x}, t) = \boldsymbol{\sigma}^{(\alpha)}(\mathbf{x}, t) : \boldsymbol{Z}^{s(\alpha)}$). The strength of each slip system is taken to evolve based on the following hardening rule [6]:

$$\dot{g}^{s(\alpha)} = h_0 \left(\frac{g_{sa}^{s(\alpha)} - g^{s(\alpha)}}{g_{sa}^{s(\alpha)} - g_0^{s(\alpha)}} \right) \sum_{s=1}^{N} |\dot{\gamma}^{s(\alpha)}| \tag{9}$$

where h_0 is the initial hardening rate, $g_0^{s(\alpha)}$ the initial strength of the s^{th} slip system, and $g_{sa}^{s(\alpha)}$ the saturation shear stress. All parameters describing the hardening are taken to be orientation independent (i.e., same for all slip systems).

Equations (5)-(9) define the reduced order microscale problem. While each part in EHM can be chosen as a whole grain or subdomain of a grain to provide different local response resolution, we use the one-part-per-grain scheme in the current work (each grain is considered a part, and n is equal to number of grains in the microstructure). The full EHM formulation recovers the representative volume problem in the classical computational homogenization approach, where each element of the RVE mesh is considered a part (i.e., n equals the number of elements). The convergence of the EHM approach with increasing model order, n has been

characterized in Ref. [39, 57]. Zhang and Oskay [60] demonstrated the capability of EHM in better capturing the local stress distributions within the polycrystalline microstructure as n increases (i.e., when a grain is subdivided into multiple parts).

2.1 EHM Computational Implementation Overview

The reduced order microscale system defined by Eqs. (5)-(9) has been implemented as a User supplied MATerial (UMAT) subroutine within the finite element solver Abaqus and is called to update the stress increment and tangent moduli at each time increment of each integration point of the macroscale discretization. The constitutive equation (Eq. (5)), along with the evolution equations for slip and hardening constitutes a nonlinear system, evaluated using the Newton-Raphson (N-R) method. Evaluating the system with the part-average stresses, $\boldsymbol{\sigma}^{(\alpha)}$ as unknowns, the system Jacobian is expressed as:

$$\mathbf{J} = \begin{bmatrix} \frac{\partial \boldsymbol{\phi}^{(1)}}{\partial \boldsymbol{\sigma}^{(1)}} & \frac{\partial \boldsymbol{\phi}^{(1)}}{\partial \boldsymbol{\sigma}^{(2)}} & \cdots & \frac{\partial \boldsymbol{\phi}^{(1)}}{\partial \boldsymbol{\sigma}^{(\bar{\alpha})}} & \cdots & \frac{\partial \boldsymbol{\phi}^{(1)}}{\partial \boldsymbol{\sigma}^{(\bar{\beta})}} & \cdots & \frac{\partial \boldsymbol{\phi}^{(1)}}{\partial \boldsymbol{\sigma}^{(n)}} \\ \frac{\partial \boldsymbol{\phi}^{(2)}}{\partial \boldsymbol{\sigma}^{(1)}} & \frac{\partial \boldsymbol{\phi}^{(2)}}{\partial \boldsymbol{\sigma}^{(2)}} & \cdots & \frac{\partial \boldsymbol{\phi}^{(2)}}{\partial \boldsymbol{\sigma}^{(\bar{\alpha})}} & \cdots & \frac{\partial \boldsymbol{\phi}^{(2)}}{\partial \boldsymbol{\sigma}^{(\bar{\beta})}} & \cdots & \frac{\partial \boldsymbol{\phi}^{(2)}}{\partial \boldsymbol{\sigma}^{(n)}} \\ \vdots & \vdots & \ddots & \vdots & \ddots & \vdots & \ddots & \vdots \\ \frac{\partial \boldsymbol{\phi}^{(\bar{\alpha})}}{\partial \boldsymbol{\sigma}^{(1)}} & \frac{\partial \boldsymbol{\phi}^{(\bar{\alpha})}}{\partial \boldsymbol{\sigma}^{(2)}} & \cdots & \frac{\partial \boldsymbol{\phi}^{(\bar{\alpha})}}{\partial \boldsymbol{\sigma}^{(\bar{\alpha})}} & \cdots & \frac{\partial \boldsymbol{\phi}^{(\bar{\alpha})}}{\partial \boldsymbol{\sigma}^{(\bar{\beta})}} & \cdots & \frac{\partial \boldsymbol{\phi}^{(\bar{\alpha})}}{\partial \boldsymbol{\sigma}^{(n)}} \\ \vdots & \vdots & \ddots & \vdots & \ddots & \vdots & \ddots & \vdots \\ \frac{\partial \boldsymbol{\phi}^{(\bar{\beta})}}{\partial \boldsymbol{\sigma}^{(1)}} & \frac{\partial \boldsymbol{\phi}^{(\bar{\beta})}}{\partial \boldsymbol{\sigma}^{(2)}} & \cdots & \frac{\partial \boldsymbol{\phi}^{(\bar{\beta})}}{\partial \boldsymbol{\sigma}^{(\bar{\alpha})}} & \cdots & \frac{\partial \boldsymbol{\phi}^{(\bar{\beta})}}{\partial \boldsymbol{\sigma}^{(\bar{\beta})}} & \cdots & \frac{\partial \boldsymbol{\phi}^{(\bar{\beta})}}{\partial \boldsymbol{\sigma}^{(n)}} \\ \vdots & \vdots & \ddots & \vdots & \ddots & \vdots & \ddots & \vdots \\ \frac{\partial \boldsymbol{\phi}^{(n)}}{\partial \boldsymbol{\sigma}^{(1)}} & \frac{\partial \boldsymbol{\phi}^{(n)}}{\partial \boldsymbol{\sigma}^{(2)}} & \cdots & \frac{\partial \boldsymbol{\phi}^{(n)}}{\partial \boldsymbol{\sigma}^{(\bar{\alpha})}} & \cdots & \frac{\partial \boldsymbol{\phi}^{(n)}}{\partial \boldsymbol{\sigma}^{(\bar{\beta})}} & \cdots & \frac{\partial \boldsymbol{\phi}^{(n)}}{\partial \boldsymbol{\sigma}^{(n)}} \end{bmatrix} \tag{10}$$

where each component is a 6×6 block expressed as:

$$\left(\frac{\partial \phi^{(\beta)}}{\partial \sigma^{(\alpha)}}\right)_{IK} = \left(\delta^{(\alpha\beta)} I_{IJ} - P_{IJ}^{(\beta\alpha)}\right) \sum_{s=1}^{N} \Omega^{s(\alpha)} Z_J^{s(\alpha)} Z_K^{s(\alpha)} + \delta^{(\alpha\beta)} \frac{M_{IK}^{(\beta)}}{\Delta t} \tag{11}$$

in which,

$$\Omega^{s(\alpha)} = \frac{\dot{\gamma}_0}{m} \frac{1}{g^{s(\alpha)}} \left(\frac{|\tau^{s(\alpha)}|}{g^{s(\alpha)}}\right)^{\frac{1-m}{m}} \tag{12}$$

Voigt notation has been employed to condense the indices (i.e., $ij \rightarrow K$ with $11 \rightarrow 1$, $22 \rightarrow 2$, $33 \rightarrow 3$, $23 \rightarrow 4$, $13 \rightarrow 5$, $12 \rightarrow 6$).

The tangent moduli is expressed as:

$$\frac{\partial \bar{\sigma}_I}{\partial \bar{\epsilon}_J} = \sum_{\alpha=1}^{N} C^{(\alpha)} \frac{\partial \sigma_I^{(\alpha)}}{\partial \bar{\epsilon}_J} \tag{13}$$

in which, $C^{(\alpha)}$ is the volume fraction of part α and each component $\frac{\partial \sigma_I^{(\alpha)}}{\partial \bar{\epsilon}_J}$ is the solution of

the linear system:

$$\sum_{\alpha=1}^{n}\Big[(\delta^{(\alpha\beta)}I_{IJ}-P_{IJ}^{(\beta\alpha)})\varphi_{JL}^{(\alpha)}+\delta^{(\alpha\beta)}\frac{M_{IL}^{(\beta)}}{\Delta t}\Big]\frac{\partial\sigma_{L}^{(\alpha)}}{\partial\bar{\epsilon}_{K}}=\frac{A_{IK}^{(\beta)}}{\Delta t} \tag{14}$$

where,

$$\varphi_{JL}^{(\alpha)}=\sum_{s=1}^{N}\frac{\dot{\gamma}_0}{m}\frac{1}{g^{s(\alpha)}}\left(\frac{\left|\tau^{s(\alpha)}\right|}{g^{s(\alpha)}}\right)^{\frac{1-m}{m}}Z_{J}^{s(\alpha)}Z_{L}^{s(\alpha)} \tag{15}$$

The linearized system in Eq. (14) has six right-hand side vectors, while the resulting matrix on the left-hand side is similar to that in Eq. (10), with the only difference that the former is evaluated using the converged stress and slip resistance while the latter is evaluated using the value at each iteration.

2.2 Analysis of EHM scalability

Most of the computational cost of solving the reduced order microscale problem comes from constructing and solving the linearized EHM system in each N-R iteration, as well as calculating the tangent moduli by solving the linear system in Eq. (14). The computational cost is therefore determined by the size of the linear system (i.e., $6n$). In what follows, we study the efficiency of EHM compared with CPFE as a function of RVE size (or alternatively the order of the EHM model as model order is tied to the number of grains in this study).

In general, the number of grains in an RVE is often on the order of a few hundred depending on the complexity of the constitutive behavior and the microstructure morphology [40, 10, 52, 5, 61]. The EHM efficiency for RVE sizes within this range is evaluated using uniaxial tension test as shown in Fig. 2(a). The macroscale mesh consists of a single hexahedron with reduced order integration regularized with hourglass stiffness. The reference CPFE analysis is performed over the fully resolved microstructure discretized with trilinear four-noded tetrahedron elements. A direct solver is used for all reference simulations. Displacement controlled loading with a total applied strain of 5% at a strain rate of 0.05/s is applied to all simulations with the initial time step size 1.0×10^{-6} s and maximum allowable step size of 0.01 s. The investigation is conducted on a series of increasing size RVEs constructed from the same microstructure morphology and discretized using the same mesh size as shown in Fig. 2(b)-(h). All simulations were conducted on the same computer (Intel I7 3.0 GHz processor, 16G RAM) without parallelization and all finished in 122 increments.

Information on the number of elements (i.e., n_{element}) and nodes (i.e., n_{node}) in each microstructure as well as the simulation times (i.e., T_{CPFE} and T_{EHM}) are listed in Table 1. Since all microstructures are constructed using the same microstructural statistics and meshed with the same element size, number of degrees of freedom (DOF) increases linearly with the total number of grains in the microstructure. For the EHMs, the DOF associated with the linearized system is $6n$. Since each grain constitutes a part, there is a linear relationship between total

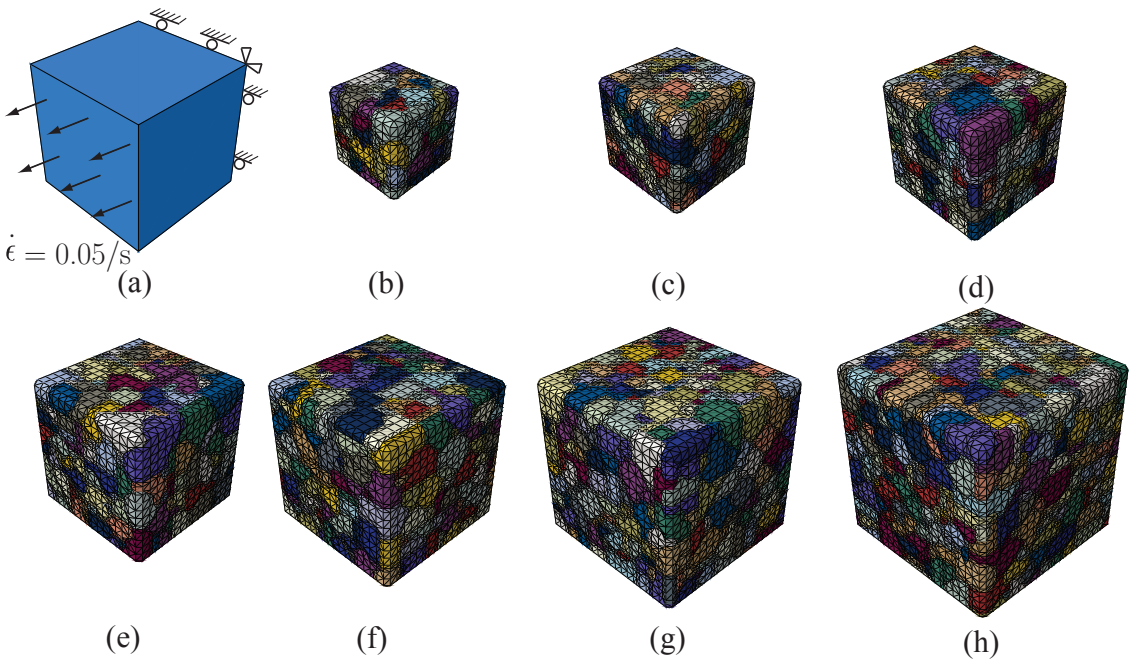

Figure 2: Schematic demonstration of (a) the boundary conditions, and (b-h) finite element mesh of RVEs used in the simulation with $n = 85, 154, 242, 347, 487, 629, 938$.

Table 1: EHM efficiency compared with direct CPFE.

n	n_{element}	n_{node}	$T_{\text{CPFE}}(s)$	$T_{\text{EHM}}(s)$	R_{DOF}	R_{Time}
85	29,369	5,627	2128.66	19.05	33.11	111.74
154	53,149	9,983	4,034.03	74.85	32.41	53.89
242	84,642	15,583	7,052.75	265.08	32.20	26.61
347	128,716	23,339	10,371.25	662.12	33.63	15.66
487	176,415	31,777	13,998.82	1,671.50	32.63	8.38
629	238,216	42,651	19,435.03	3,434.18	33.90	5.66
938	337,818	60,122	29,451.22	11,240.56	32.05	2.62

number of DOF and number of grains for the EHMs as well. Using the current microstructure statistics and mesh size, each grain is discretized into approximately 350 trilinear tetrahedron elements. The ratio of the number of DOF between CPFE and EHM (i.e., R_{DOF}) is approximately 33 for all microstructures.

The simulation times of CPFE and EHM using different microstructures are compared in Table 1 and Fig. 3. While the simulation time of CPFE increases roughly linearly with number of grains (since calculations on integration points dominate cost compared with solving the global system in the context of nonlinear FE analysis), simulation time of EHM scales approximately with n^3. Consequently, the efficiency of EHM compared with CPFE (i.e., speedup of EHM compared to CPFE, defined by the ratio between simulation time of CPFE and EHM, R_{Time}, in Table 1) reduces as a function of microstructure size (Fig. 4(a)). Clearly,

maintaining high efficiency of reduced order models within this range of RVE sizes is critical and motivates the accelerated reduced order model formulation discussed below.

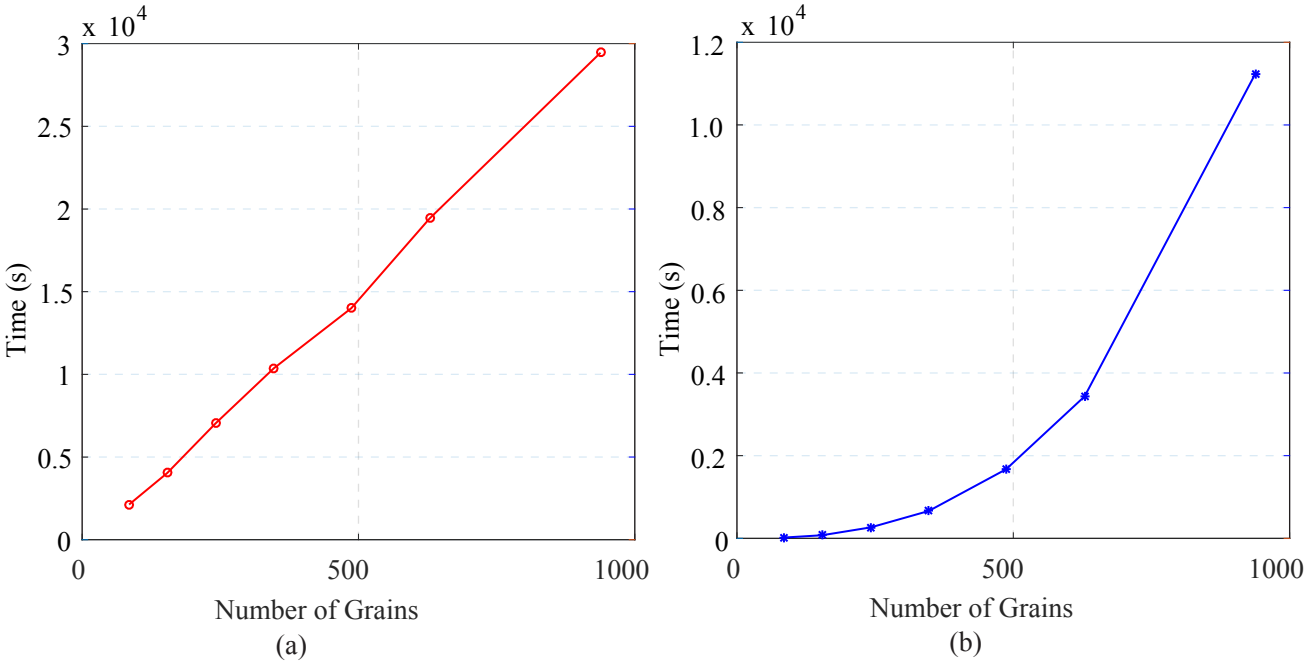

Figure 3: Simulation time as a function of microstructure size using (a) CPFE; and (b) EHM models. The ratio of DOF between CPFE and EHM simulations is approximately constant as a function of RVE size (see Table 1).

The primary cause for the efficiency degradation with increasing number of grains is the structure of the linear system in N-R iterations when solving the reduced order system and calculating the tangent stiffness. It is straightforward to see that the above linear system (Eq. (10)) is dense and unsymmetric, with a dimension of $6n$. The number of floating-point operations (FLOPs) of solving a dense unsymmetric linear system of dimension $6n$ using a direct solver (e.g., LAPACK LU decomposition routines) is $0.67(6n)^3 = 144.72n^3$ [7]. This explains the cubic increase in simulation time for the EHM.

Remark 1. *We also investigate the effect of using an iterative solver in the evaluation of the EHM model. Iterative solvers are preferred for large systems, where memory resources are not sufficient for a direct solver, while direct solvers are advantageous in small and moderate sized problems. Direct solvers are also advantageous for problems with multiple right-hand side vectors since numerical factorization (major computational cost) needs to be conducted only once. In contrast, iterative solvers evaluate each right-hand side as a separate problem and the cost is proportional to the number of right-hand sides. Flexible General Minimum Residual method (FGMRES) [46] implemented in Intel MKL library [2] is employed in this study. The reported results are with Gauss-Seidel pre-conditioning since it provides the highest efficiency among common preconditions (Jacobi, successive over relaxation, symmetric successive over relaxation and incomplete LU decomposition-based pre-conditioning) in the current study.*

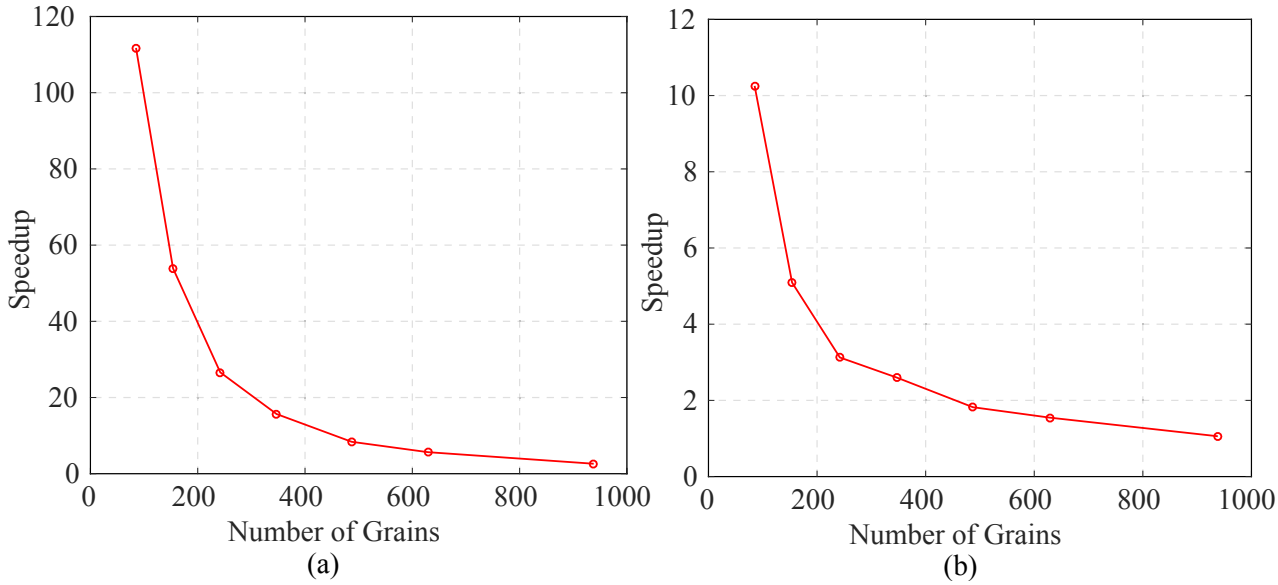

Figure 4: Efficiency of EHM compared with CPFE as a function of RVE size using: (a) direct solver; and (b) iterative solver to evaluate the reduced order system.

Table 2: Simulation time of EHM using FGMRES.

n	85	154	242	347	487	629	938
Time (s)	207.59	792.27	2,255.92	3,992.20	7,686.17	12,566.87	27,820.14

Simulation time of EHM using FGMRES as linear solver is listed in Table 2 and the efficiency of EHM using FGMRES compared with CPFE is plotted in Fig. 4(b). EHM using iterative solver is less efficient than direct solver in the current example, but shows similar EHM efficiency degradation as a function of RVE size.

3 Sparse EHM models.

We seek to develop reduced order models that increase efficiency compared with the full EHM, and have better scalability. This is achieved by introducing sparsity into the Jacobian matrix of the linearized EHM system. The off-diagonal components that account for the interaction between two arbitrary grains $\bar{\alpha}$ and $\bar{\beta}$ ($\bar{\beta} \neq \bar{\alpha}$) takes the form:

$$\left(\frac{\partial \phi^{(\bar{\beta})}}{\partial \sigma^{(\bar{\alpha})}}\right)_{IK} = -P_{IJ}^{(\bar{\beta}\bar{\alpha})} \sum_{s=1}^{N} \Omega^{s(\bar{\alpha})} Z_J^{s(\bar{\alpha})} Z_K^{s(\bar{\alpha})}; \;\; \bar{\beta} \neq \bar{\alpha} \tag{16}$$

The interaction term vanishes if $\mathbf{P}^{(\bar{\beta}\bar{\alpha})} = \mathbf{0}$ is set to zero (similarly $\frac{\partial \boldsymbol{\phi}^{(\bar{\alpha})}}{\partial \boldsymbol{\sigma}^{(\bar{\beta})}} = \mathbf{0}$ if $\mathbf{P}^{(\bar{\alpha}\bar{\beta})} = \mathbf{0}$). By neglecting the grain-to-grain interaction, two 6×6 zero blocks are introduced into the Jacobian matrix (Eq. (10)). A structurally symmetric sparse linear system (zero-valued components distributed symmetrically across the diagonal) is obtained through neglected interactions for a

group of selected grain pairs. The sparsity of the resulting system is naturally determined by the extent of neglected interactions. The consequence of partial consideration of grain-to-grain interactions are provided in the next section.

Neglecting all grain interactions (i.e., $\mathbf{P}^{(\alpha\beta)} = \mathbf{0}$ for $\alpha = 1, 2, ..., n,,\ \beta = 1, 2, ..., n, \alpha \neq \beta$) results in a diagonal structure, providing the maximum possible computational efficiency. The resulting EHM system has n 6×6 (in 3-D) independent systems, which can be evaluated with $0.67 \times (6)^3 \times n = 144.72n$ FLOPs. The accuracy and efficiency characteristics of this model are similar to the Taylor model. Neglecting p pairs of grain-to-grain interactions results in a sparse system with the sparsity $S = 2p/n^2$.

The goal is to obtain EHM models that exhibit the highest possible sparsity without significantly compromising on the computational accuracy compared to the full EHM model. To this end, we next establish (1) the mathematical and physical consequences of eliminating certain grain-to-grain interactions; (2) the numerical procedures to determine the interactions to keep in the resulting sparse system; and (3) the numerical methodology for efficient evaluation of the sparse EHM models.

3.1 Coefficient tensors considering partial interactions

In the context of uniform transformation field analysis, Dvorak and Benveniste [14, 15] derived the following properties for the coefficient tensors:

$$\text{Kinematic consistency} : \sum_{\alpha=1}^{n} \mathbf{P}^{(\beta\alpha)} = \mathbf{I} - \mathbf{A}^{(\beta)} \tag{17}$$

$$\text{Simultaneous iso-stress/strain condition} : \sum_{\alpha=1}^{n} \mathbf{P}^{(\beta\alpha)}\mathbf{M}^{(\alpha)} = \mathbf{0} \tag{18}$$

$$\text{Elastic reciprocity} : c^{(\beta)}\mathbf{P}^{(\beta\alpha)}\mathbf{M}^{(\alpha)} = c^{(\alpha)}\mathbf{M}^{(\beta)}\mathbf{P}^{(\alpha\beta),T} \tag{19}$$

$$\text{Strain compatibility} : \sum_{\alpha=1}^{n} c^{(\alpha)}\mathbf{P}^{(\alpha\beta)} = \mathbf{0} \tag{20}$$

where, the strain compatibility comes from the requirement that the average of strains in each part is equal to the macroscale strain; the elasticity reciprocity is derived from the elastic reciprocal theorem; and simultaneous iso-stress/strain condition and kinematic consistency are obtained considering a special case where the whole domain is subjected to uniform strain

and stress. In addition, the concentration tensors $\mathbf{A}^{(\alpha)}$ satisfy the Hill relation [18]:

$$\sum_{\alpha=1}^{n} c^{(\alpha)} \mathbf{A}^{(\alpha)} = \mathbf{I} \tag{21}$$

The new set of coefficient tensors is derived from the coefficient tensors of the full EHM by selectively considering grain-to-grain interactions (setting the transmitted interaction tensors to be zero between grains where interaction are neglected) while adopting the concept of mass lumping in finite element analysis to lump the neglected transmitted interaction tensors onto the self-induced terms (i.e., contributions from the off-diagonal components in Eq. (10) are lumped to the diagonal terms) and enforcing some of the constraints in Eqs. (17)-(21). By this approach, two models that either enforce the kinematic consistency and strain compatibility, or kinematic consistency and simultaneous iso-stress/strain condition are formulated. In what follows, these models are referred to as strain compatibility constrained sparse EHM (ϵ-EHM) and iso-stress/strain constrained sparse EHM (σ-EHM), respectively.

Below, the lumping procedures to obtain the ϵ-EHM and σ-EHM by eliminating the interaction between a single pair of reduced model grains ($\bar{\alpha}$ and $\bar{\beta}$) are provided. These procedures are performed for all reduced model grain pairs, whose interactions are to be neglected.

3.1.1 Strain compatibility constrained sparse EHM (ϵ-EHM)

Consider a pair of grains $\bar{\alpha}$ and $\bar{\beta}$, between which the interaction is to be neglected. Let $\mathbf{P}'^{(\bar{\alpha}\bar{\beta})}$ denote the new sparse set of interaction tensors, which are set to zero:

$$\mathbf{P}'^{(\bar{\alpha}\bar{\beta})} = 0, \quad \mathbf{P}'^{(\bar{\beta}\bar{\alpha})} = 0 \tag{22}$$

The compliance tensors remain identical to those in the full EHM:

$$\mathbf{M}'^{(\alpha)} = \mathbf{M}^{(\alpha)}, \ \alpha = 1, 2, ..., n \tag{23}$$

To enforce the strain compatibility (Eq. (20)), the effect of the neglected transmitted interaction tensors are lumped to the self-induced ones:

$$\mathbf{P}'^{(\alpha\beta)} = \begin{cases} \mathbf{0} & \{\alpha,\beta\} = \{\bar{\alpha},\bar{\beta}\} \text{ or } \{\alpha,\beta\} = \{\bar{\beta},\bar{\alpha}\} \\ \mathbf{P}^{(\bar{\alpha}\bar{\alpha})} + \frac{c^{(\bar{\beta})}}{c^{(\bar{\alpha})}} \mathbf{P}^{(\bar{\beta}\bar{\alpha})} & \{\alpha,\beta\} = \{\bar{\alpha},\bar{\alpha}\} \\ \mathbf{P}^{(\bar{\beta}\bar{\beta})} + \frac{c^{(\bar{\alpha})}}{c^{(\bar{\beta})}} \mathbf{P}^{(\bar{\alpha}\bar{\beta})} & \{\alpha,\beta\} = \{\bar{\beta},\bar{\beta}\} \\ \mathbf{P}^{(\alpha\beta)} & \text{otherwise} \end{cases} \tag{24}$$

Substituting Eq. (24) into Eq. (17), the new concentration tensors are obtained as:

$$\mathbf{A}'^{(\alpha)} = \begin{cases} \mathbf{A}^{(\alpha)} & \alpha \notin \{\bar{\alpha}, \bar{\beta}\} \\ \mathbf{A}^{(\bar{\alpha})} + \mathbf{P}^{(\bar{\alpha}\bar{\beta})} - \frac{c^{(\bar{\beta})}}{c^{(\bar{\alpha})}} \mathbf{P}^{(\bar{\beta}\bar{\alpha})} & \alpha = \bar{\alpha} \\ \mathbf{A}^{(\bar{\beta})} + \mathbf{P}^{(\bar{\beta}\bar{\alpha})} - \frac{c^{(\bar{\alpha})}}{c^{(\bar{\beta})}} \mathbf{P}^{(\bar{\alpha}\bar{\beta})} & \alpha = \bar{\beta} \end{cases} \tag{25}$$

and it is trivial to verify that Eq. (21) holds for the new concentration tensors:

$$\sum_{\alpha=1}^{n} c^{(\alpha)} \mathbf{A}'^{(\alpha)} = \sum_{\alpha=1}^{n} c^{(\alpha)} \mathbf{A}^{(\alpha)} = \mathbf{I} \tag{26}$$

We next investigate the impact of the above lumping procedure on the elastic reciprocity and the simultaneous iso-stress/strain condition of the resulting system. Substituting the new coefficient tensors (Eqs. (23) and (24)) into the elastic reciprocity (Eq. (19)), we obtain:

$$c^{(\beta)} \mathbf{P}'^{(\beta\alpha)} \mathbf{M}'^{(\alpha)} = c^{(\beta)} \mathbf{P}^{(\beta\alpha)} \mathbf{M}^{(\alpha)} = c^{(\alpha)} \mathbf{M}^{(\beta)} \mathbf{P}^{(\alpha\beta),T} = c^{(\alpha)} \mathbf{M}'^{(\beta)} \mathbf{P}'^{(\alpha\beta),T}; \quad \alpha \notin \{\bar{\alpha}, \bar{\beta}\} \text{ and } \beta \notin \{\bar{\alpha}, \bar{\beta}\} \tag{27}$$

$$c^{(\bar{\beta})} \mathbf{P}'^{(\bar{\beta}\bar{\alpha})} \mathbf{M}'^{(\bar{\alpha})} = 0 = c^{(\bar{\alpha})} \mathbf{M}'^{(\bar{\beta})} \mathbf{P}'^{(\bar{\alpha}\bar{\beta}),T}; \ \{\alpha, \beta\} = \{\bar{\alpha}, \bar{\beta}\} \tag{28}$$

However, in the case of $\{\alpha, \beta\} = \{\bar{\alpha}, \bar{\alpha}\}$ or $\{\alpha, \beta\} = \{\bar{\beta}, \bar{\beta}\}$, the reciprocity condition implies:

$$c^{(\bar{\alpha})} \mathbf{P}'^{(\bar{\alpha}\bar{\alpha})} \mathbf{M}'^{(\bar{\alpha})} = c^{(\bar{\alpha})} \mathbf{M}'^{(\bar{\alpha})} \mathbf{P}'^{(\bar{\alpha}\bar{\alpha}),T} \tag{29}$$

$$c^{(\bar{\beta})} \mathbf{P}'^{(\bar{\beta}\bar{\beta})} \mathbf{M}'^{(\bar{\beta})} = c^{(\bar{\beta})} \mathbf{M}'^{(\bar{\beta})} \mathbf{P}'^{(\bar{\beta}\bar{\beta}),T} \tag{30}$$

Substituting Eq. (24) and the elastic reciprocity into Eqs. (29) and (30) yields:

$$\begin{aligned} \mathbf{P}^{(\bar{\beta}\bar{\alpha})} \mathbf{M}^{(\bar{\alpha})} - \mathbf{M}^{(\bar{\alpha})} \mathbf{P}^{(\bar{\beta}\bar{\alpha}),T} = 0 \\ \mathbf{P}^{(\bar{\alpha}\bar{\beta})} \mathbf{M}^{(\bar{\beta})} - \mathbf{M}^{(\bar{\beta})} \mathbf{P}^{(\bar{\alpha}\bar{\beta}),T} = 0 \end{aligned} \tag{31}$$

which are not guaranteed.

Substituting the new coefficient tensors (Eqs. (23) and (24)) into the simultaneous iso-stress/strain condition, yields:

$$\sum_{\alpha=1}^{n} \mathbf{P}'^{(\beta\alpha)} \mathbf{M}'^{(\alpha)} = \sum_{\alpha=1}^{n} \mathbf{P}^{(\beta\alpha)} \mathbf{M}^{(\alpha)} = \mathbf{0}; \ \beta \notin \{\bar{\alpha}, \bar{\beta}\} \tag{32}$$

$$\sum_{\alpha=1}^{n} \mathbf{P}'^{(\bar{\alpha}\alpha)} \mathbf{M}^{(\alpha)} = \frac{1}{c^{(\bar{\alpha})}} \Big(c^{(\bar{\beta})} \mathbf{P}^{(\bar{\beta}\bar{\alpha})} \mathbf{M}^{(\bar{\alpha})} - c^{(\bar{\alpha})} \mathbf{P}^{(\bar{\alpha}\bar{\beta})} \mathbf{M}^{(\bar{\beta})} \Big) \tag{33}$$

$$\sum_{\alpha=1}^{n} \mathbf{P}'^{(\bar{\beta}\alpha)} \mathbf{M}^{(\alpha)} = \frac{1}{c^{(\bar{\beta})}} \Big(c^{(\bar{\alpha})} \mathbf{P}^{(\bar{\alpha}\bar{\beta})} \mathbf{M}^{(\bar{\beta})} - c^{(\bar{\beta})} \mathbf{P}^{(\bar{\beta}\bar{\alpha})} \mathbf{M}^{(\bar{\alpha})} \Big) \tag{34}$$

Substituting the elastic reciprocity into Eqs. (33) and (34), again leads to Eq. (31). Therefore $\epsilon-$EHM fully satisfies the constraints in Eqs. (17) and (20), whereas the constraints in Eqs. (18) and (19) are partially satisfied.

3.1.2 Simultaneous iso-stress/strain constrained sparse EHM (σ-EHM)

In addition to the strain compatibility constrained sparse EHM, we propose an alternative formulation, where the kinematic consistency and simultaneous iso-stress/strain condition are satisfied (denoted as σ-EHM). In σ-EHM, Eqs. (17) and (18) are retained.

The interaction tensors (after neglecting the interaction between grain $\bar{\alpha}$ and $\bar{\beta}$) are chosen such that the kinetic consistency in Eq. (18) is satisfied as:

$$\mathbf{P}'^{(\alpha\beta)} = \begin{cases} \mathbf{0} & \{\alpha,\beta\} = \{\bar{\alpha},\bar{\beta}\} \text{ or } \{\alpha,\beta\} = \{\bar{\beta},\bar{\alpha}\} \\ \mathbf{P}^{(\bar{\alpha}\bar{\alpha})} + \frac{c^{(\bar{\beta})}}{c^{(\bar{\alpha})}}\mathbf{M}^{(\bar{\alpha})}\mathbf{P}^{(\bar{\beta}\bar{\alpha}),T}\mathbf{M}^{(\bar{\alpha}),-1} & \{\alpha,\beta\} = \{\bar{\alpha},\bar{\alpha}\} \\ \mathbf{P}^{(\bar{\beta}\bar{\beta})} + \frac{c^{(\bar{\alpha})}}{c^{(\bar{\beta})}}\mathbf{M}^{(\bar{\beta})}\mathbf{P}^{(\bar{\alpha}\bar{\beta}),T}\mathbf{M}^{(\bar{\beta}),-1} & \{\alpha,\beta\} = \{\bar{\beta},\bar{\beta}\} \\ \mathbf{P}^{(\alpha\beta)} & \text{otherwise} \end{cases} \tag{35}$$

Substituting Eq. (35) into Eq. (17), the new concentration tensors are calculated as:

$$\mathbf{A}'^{(\alpha)} = \begin{cases} \mathbf{A}^{(\alpha)} & \alpha \notin \{\bar{\alpha},\bar{\beta}\} \\ \mathbf{A}^{(\bar{\alpha})} + \mathbf{P}^{(\bar{\alpha}\bar{\beta})} - \frac{c^{(\bar{\beta})}}{c^{(\bar{\alpha})}}\mathbf{M}^{(\bar{\alpha})}\mathbf{P}^{(\bar{\beta}\bar{\alpha})}\mathbf{M}^{(\bar{\alpha}),-1} & \alpha = \bar{\alpha} \\ \mathbf{A}^{(\bar{\beta})} + \mathbf{P}^{(\bar{\beta}\bar{\alpha})} - \frac{c^{(\bar{\alpha})}}{c^{(\bar{\beta})}}\mathbf{M}^{(\bar{\beta})}\mathbf{P}^{(\bar{\alpha}\bar{\beta})}\mathbf{M}^{(\bar{\beta}),-1} & \alpha = \bar{\beta} \end{cases} \tag{36}$$

We next investigate the impact of the above lumping procedure on the elastic reciprocity and strain compatibility of the resulting system. Substituting Eqs. (35) and (36) into Eq. (19) yields:

$$c^{(\beta)}\mathbf{P}'^{(\beta\alpha)}\mathbf{M}^{(\alpha)} - c^{(\alpha)}\mathbf{M}^{(\beta)}\mathbf{P}'^{(\alpha\beta),T} = c^{(\beta)}\mathbf{P}^{(\beta\alpha)}\mathbf{M}^{(\alpha)} - c^{(\alpha)}\mathbf{M}^{(\beta)}\mathbf{P}^{(\alpha\beta),T} = \mathbf{0};\ \beta \notin \{\bar{\alpha},\bar{\beta}\} \tag{37}$$

$$\begin{aligned} c^{(\bar{\beta})}\mathbf{P}'^{(\bar{\beta}\bar{\beta})}\mathbf{M}^{(\bar{\beta})} - c^{(\bar{\beta})}\mathbf{M}^{(\bar{\beta})}\mathbf{P}'^{(\bar{\beta}\bar{\beta}),T} = c^{(\bar{\beta})}(\mathbf{P}^{(\bar{\beta}\bar{\beta})}\mathbf{M}^{(\bar{\beta})} - \mathbf{M}^{(\bar{\beta})}\mathbf{P}^{(\bar{\beta}\bar{\beta}),T}) + \\ c^{(\bar{\alpha})}\Big(\mathbf{M}^{(\bar{\beta})}\mathbf{P}^{(\bar{\alpha}\bar{\beta}),T} - \mathbf{P}^{(\bar{\alpha}\bar{\beta})}\mathbf{M}^{(\bar{\beta})}\Big) \end{aligned} \tag{38}$$

$$\begin{aligned} c^{(\bar{\alpha})}\mathbf{P}'^{(\bar{\alpha}\bar{\alpha})}\mathbf{M}^{(\bar{\alpha})} - c^{(\bar{\alpha})}\mathbf{M}^{(\bar{\alpha})}\mathbf{P}'^{(\bar{\alpha}\bar{\alpha}),T} = c^{(\bar{\alpha})}(\mathbf{P}^{(\bar{\alpha}\bar{\alpha})}\mathbf{M}^{(\bar{\alpha})} - \mathbf{M}^{(\bar{\alpha})}\mathbf{P}^{(\bar{\alpha}\bar{\alpha}),T}) + \\ c^{(\bar{\beta})}\Big(\mathbf{M}^{(\bar{\alpha})}\mathbf{P}^{(\bar{\beta}\bar{\alpha}),T} - \mathbf{P}^{(\bar{\beta}\bar{\alpha})}\mathbf{M}^{(\bar{\alpha})}\Big) \end{aligned} \tag{39}$$

Utilizing the elastic reciprocity, the above equations are written as:

$$\begin{aligned} c^{(\bar{\beta})}\mathbf{P}'^{(\bar{\beta}\bar{\beta})}\mathbf{M}^{(\bar{\beta})} - c^{(\bar{\beta})}\mathbf{M}^{(\bar{\beta})}\mathbf{P}'^{(\bar{\beta}\bar{\beta}),T} &= c^{(\bar{\alpha})}\Big(\mathbf{M}^{(\bar{\beta})}\mathbf{P}^{(\bar{\alpha}\bar{\beta}),T} - \mathbf{P}^{(\bar{\alpha}\bar{\beta})}\mathbf{M}^{(\bar{\beta})}\Big) \\ c^{(\bar{\alpha})}\mathbf{P}'^{(\bar{\alpha}\bar{\alpha})}\mathbf{M}^{(\bar{\alpha})} - c^{(\bar{\alpha})}\mathbf{M}^{(\bar{\alpha})}\mathbf{P}'^{(\bar{\alpha}\bar{\alpha}),T} &= c^{(\bar{\beta})}\Big(\mathbf{M}^{(\bar{\alpha})}\mathbf{P}^{(\bar{\beta}\bar{\alpha}),T} - \mathbf{P}^{(\bar{\beta}\bar{\alpha})}\mathbf{M}^{(\bar{\alpha})}\Big) \end{aligned} \tag{40}$$

which results in the same constraints as in Eq. (31) to ensure reciprocity.

Substituting the new coefficient tensors (Eqs. (35) and (36)) into the strain compatibility (Eq. (20)) yields:

$$\sum_{\alpha=1}^{N} c^{(\alpha)}\mathbf{P}'^{(\alpha\beta)} = \sum_{\alpha=1}^{N} c^{(\alpha)}\mathbf{P}^{(\alpha\beta)} = \mathbf{0};\ \beta \notin \{\bar{\alpha}, \bar{\beta}\} \tag{41}$$

$$\sum_{\alpha=1}^{N} c^{(\alpha)}\mathbf{P}'^{(\alpha\bar{\beta})} = c^{(\bar{\alpha})}\mathbf{M}^{(\bar{\beta})}\mathbf{P}^{(\bar{\alpha}\bar{\beta}),T}\mathbf{M}^{(\bar{\beta}),-1} - c^{(\bar{\alpha})}\mathbf{P}^{(\bar{\alpha}\bar{\beta})} \tag{42}$$

$$\sum_{\alpha=1}^{N} c^{(\alpha)}\mathbf{P}'^{(\alpha\bar{\alpha})} = c^{(\bar{\beta})}\mathbf{M}^{(\bar{\alpha})}\mathbf{P}^{(\bar{\beta}\bar{\alpha}),T}\mathbf{M}^{(\bar{\alpha}),-1} - c^{(\bar{\beta})}\mathbf{P}^{(\bar{\beta}\bar{\alpha})} \tag{43}$$

Considering Eq. (57) and the elastic reciprocity, the above equations are written as:

$$\begin{aligned}
\sum_{\alpha=1}^{N} c^{(\alpha)}\mathbf{P}'^{(\alpha\bar{\beta})} &= c^{(\bar{\beta})}\mathbf{P}^{(\bar{\beta}\bar{\alpha})}(\mathbf{M}^{(\bar{\alpha})}\mathbf{M}^{(\bar{\beta}),-1} - \mathbf{I}) \\
\sum_{\alpha=1}^{N} c^{(\alpha)}\mathbf{P}'^{(\alpha\bar{\alpha})} &= c^{(\bar{\alpha})}\mathbf{P}^{(\bar{\alpha}\bar{\beta})}(\mathbf{M}^{(\bar{\beta})}\mathbf{M}^{(\bar{\alpha}),-1} - \mathbf{I})
\end{aligned} \tag{44}$$

which are not guaranteed. Therefore $\sigma-$EHM fully satisfies the constraints in Eqs. (17) and (18), whereas the constraints in Eqs. (19) and (20) are partially satisfied.

Remark 2. *ϵ-EHM can be considered as an intermediate model between the Taylor model and the full EHM. To demonstrate this point, we first consider 0-layer ϵ-EHM for grain $\bar{\alpha}$ only (i.e., neglect interactions between grain $\bar{\alpha}$ and all other grains while other interactions are retained). Following Eq.* (25)*, the concentration tensors not related with part $\bar{\alpha}$ remain unchanged while the one related with part $\bar{\alpha}$ becomes:*

$$\begin{aligned}
\mathbf{A}'^{(\bar{\alpha})} =& \mathbf{A}^{(\bar{\alpha})} + \sum_{\beta=1}^{n}\left(\mathbf{P}^{(\bar{\alpha}\beta)} - \frac{c^{(\beta)}}{c^{(\bar{\alpha})}}\mathbf{P}^{(\beta\bar{\alpha})}\right) \\
=& \mathbf{A}^{(\bar{\alpha})} + \sum_{\beta=1}^{n}\mathbf{P}^{(\bar{\alpha}\beta)} - \sum_{\beta=1}^{n}\left(\frac{c^{(\beta)}}{c^{(\bar{\alpha})}}\mathbf{P}^{(\beta\bar{\alpha})}\right)
\end{aligned} \tag{45}$$

Substituting the kinematic consistency and strain compatibility into the above equation, we have:

$$\mathbf{A}'^{(\bar{\alpha})} = \mathbf{I} \tag{46}$$

While the interaction tensors not related with part $\bar{\alpha}$ remain unchanged according to Eq. (24)*, the new interactions related with part $\bar{\alpha}$ are calculated as:*

$$\mathbf{P}'^{(\bar{\alpha},\beta)} = \mathbf{P}'^{(\beta,\bar{\alpha})} = \mathbf{0};\ \beta = 1, 2, ..., \bar{\alpha}-1, \bar{\alpha}+1, ..., n \tag{47}$$

$$\mathbf{P}'^{(\bar{\alpha},\bar{\alpha})} = \mathbf{P}^{(\bar{\alpha},\bar{\alpha})} + \sum_{\beta=1,\ \beta\neq\bar{\alpha}}^{n}\frac{c^{(\bar{\beta})}}{c^{(\bar{\alpha})}}\mathbf{P}^{(\bar{\beta}\bar{\alpha})} = \sum_{\beta=1}^{n}\frac{c^{(\bar{\beta})}}{c^{(\bar{\alpha})}}\mathbf{P}^{(\bar{\beta}\bar{\alpha})} \tag{48}$$

which, by considering the strain compatibility equation leads to:

$$\mathbf{P}'^{(\bar{\alpha},\beta)} = \mathbf{P}'^{(\beta,\bar{\alpha})} = \mathbf{0};\ \beta = 1, 2, ..., n \tag{49}$$

Since the above derivation only employs the kinematic consistency and strain compatibility, which always hold for $\epsilon-$EHM coefficient tensors, neglecting interaction between all grains by propagating the above operations on part $\bar{\alpha}$ to all parts leads to:

$$\mathbf{A}'^{(\alpha)} = \mathbf{I};\ \alpha = 1, 2, ..., n \tag{50}$$

and

$$\mathbf{P}'^{(\alpha,\beta)} = \mathbf{0};\ \alpha = 1, 2, ..., n,\ \beta = 1, 2, ..., n \tag{51}$$

which results in a diagonal structure in Eq. (11) *and recovers the classical Taylor model.*

3.2 A consistent grain clustering scheme

The performance of the proposed accelerated EHM models clearly depends on the appropriate choice of the interactions to be kept within the material microstructure. In the current manuscript, we employ a nearest neighbor algorithm to consistently eliminate weak interactions between grains that are far away from each other.

The coefficient tensors $\mathbf{P}^{(\alpha\beta)}$ represent strains in grain α caused by a unit strain applied on grain β. $\mathbf{P}^{(\alpha\beta)}$ is typically larger when the two grains are close to each other and decreases if they are away from each other. Therefore, interactions between those grains that are far from each other are neglected. Two possibilities exist for choosing the interactions to be kept: (1) distance-based; and (2) neighborhood-based. The distance-based selection accounts for the interactions between grains that are within a prescribed distance from each other. In contrast, the neighborhood-based selection relies on grain connectivity. The distance-based and neighborhood-based algorithms are nearly identical when microstructures with uniform grain sizes are considered. Significant differences could exist in microstructures with multi-modal size distributions. It may also be possible to consider a "magnitude-based criterion", where the magnitude of the coefficient tensors (defined, for instance, as the discrete norm of the coefficient tensor) compared to a tolerance determined based on the magnitude of strong interactions). In this study, the neighborhood-based selection strategy is employed as further described below.

Let $\Theta_1^{(\alpha)}$ denote the domain of all grains in the immediate neighborhood of the grain, α, with domain, $\Theta^{(\alpha)}$ and constitutes the primary influence zone of grain α. The immediate neighborhood of $\Theta_1^{(\alpha)}$ is denoted as $\Theta_2^{(\alpha)}$ and constitutes the secondary influence zone of grain α. Following the same argument for higher order influence zones, n_c-layer grain cluster for

grain α is defined as:

$$\Omega_{n_c}^{(\alpha)} = \Theta^{(\alpha)} \cup \bigcup_{i=1}^{n_c} \Theta_i^{(\alpha)} \tag{52}$$

The algorithm for constructing the grain clusters is schematically illustrated using a simplified 2D microstructure discretization as shown in Fig. 5. The index of each grain is illustrated in Fig. 5(a). For each grain within the microstructure, the boundary nodes are identified first (Fig. 5(b)). An element connectivity-based search is then conducted to identify all grains that contain at least one of the boundary nodes of $\Theta^{(\alpha)}$ to build $\Theta_1^{(\alpha)}$ (Fig. 5(c)). To build the second layer of neighbors, $\Theta_2^{(\alpha)}$, the above process is repeated by replacing $\Theta^{(\alpha)}$ with $\Theta_1^{(\alpha)}$ (Fig. 5(d)). Due to the periodicity condition, grains that reside near the two opposing sides (2D) or surfaces (3D) of the microstructure are considered as neighbors. Typical grain cluster patterns for different grains of this idealized 2D microstructure are shown in Fig. 6. Figure 7 illustrates the resulting one-layer and two-layer grain clusters in the context of a more realistic polycrystal microstructure topology.

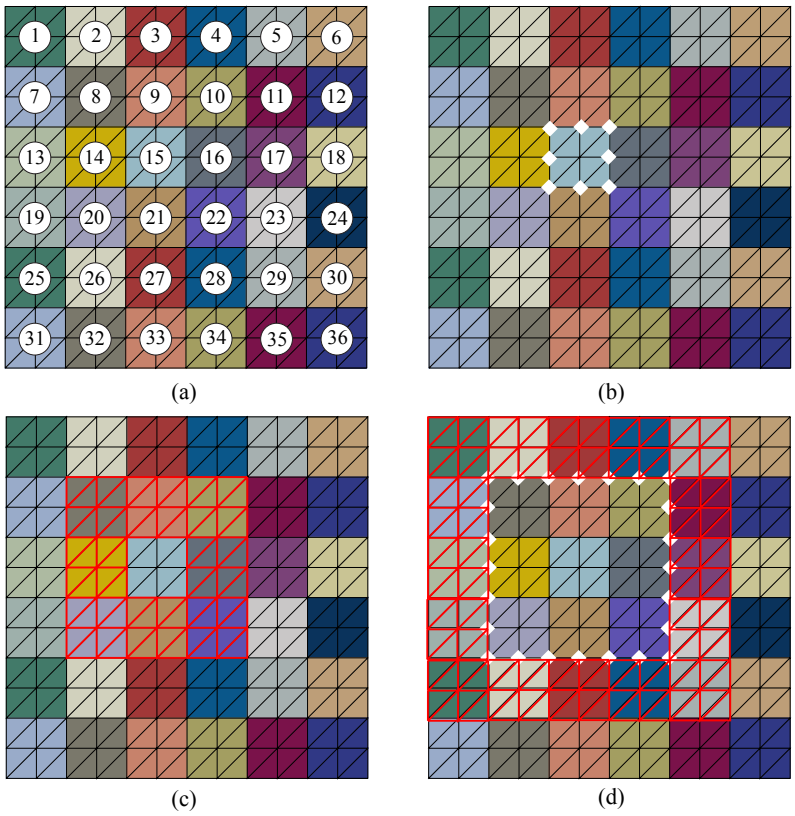

Figure 5: Schematic demonstration of the grain-clustering scheme in 2D: (a) mesh of the RVE with grain index; (b) identify the boundary nodes of the target grain, grain 15; (c) identify grains that contains the boundary nodes to identify the first layer of neighbor, $\Theta_1^{(15)}$; (d) find boundary nodes of the first layer neighbor, $\Theta_1^{(15)}$ to identify the second layer neighbor, $\Theta_2^{(15)}$.

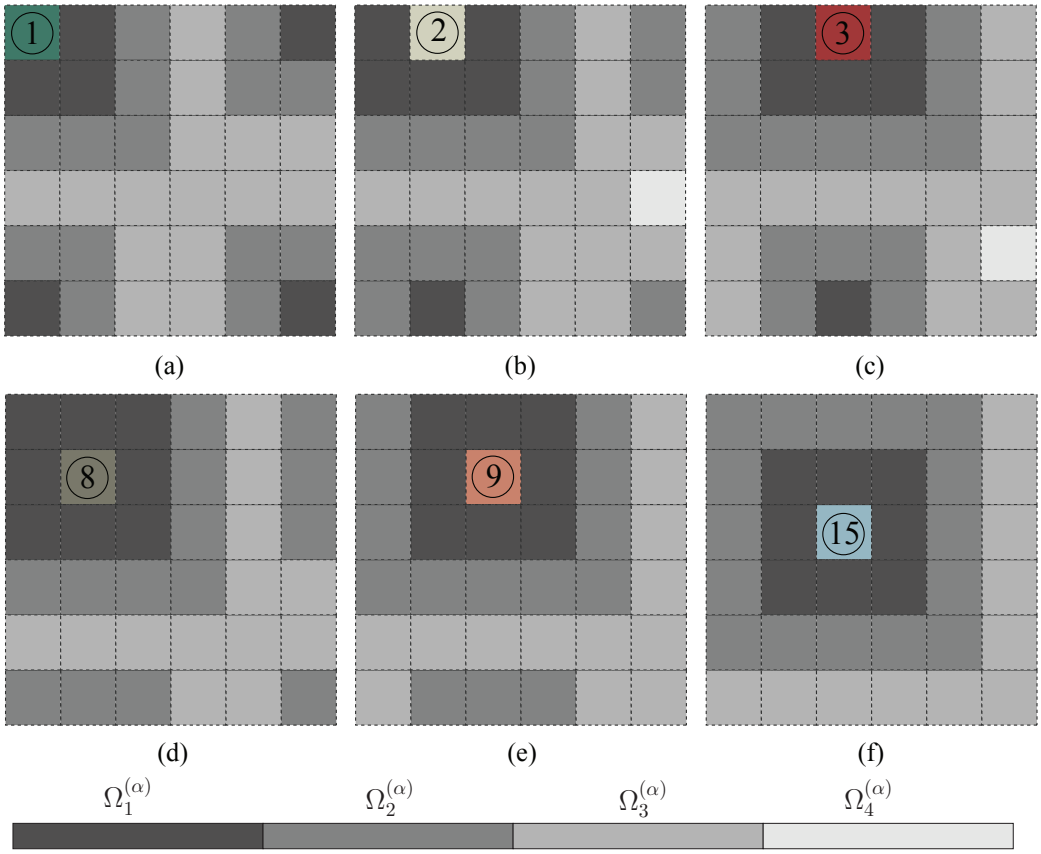

Figure 6: Grain clusters for: (a) grain 1; (b) grain 2; (c) grain 3; (d) grain 8; (e) grain 9; (f) grain 15.

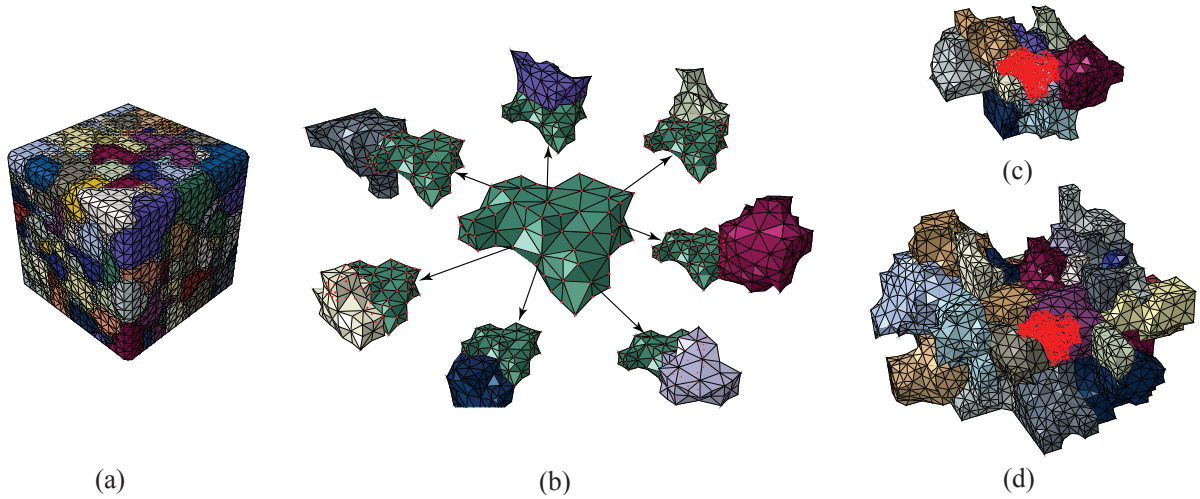

Figure 7: Schematic illustration of the grain clustering in 3D: (a) full microstructure; (b) first layer neighbor identification for the center grain (green colored); (c)-(d) identified one-layer and two-layer grain cluster for center grain (red-highlighted).

4 Computational implementation

The nonlinear numerical procedures for the sparse EHM models are similar to the full EHM (detailed in Ref. [60]), where the reduced order system is solved using the N-R process at each increment and each integration point of the macroscale analysis to update the stress and internal state variables (e.g., slip resistance) in each part. The focus of the current section is efficiently utilizing the sparse solver in the evaluation of the linearized system at each N-R iteration as well as the calculation of the tangent moduli.

4.1 Linear solution procedure for accelerated sparse EHMs

The characteristics of the linearized equations of the sparse EHM system are exploited to efficiently evaluate the reduced order models. In particular, we leverage the structural symmetry, sparsity, compressed storage and reordering of the equation system for computational efficiency.

Figures 8(a) and (b) show sparsity patterns of the linearized systems for the one-layer and two-layer sparse EHMs using the microstructure with 487 grains (Fig. 2(f)). The structural symmetry is clear when we zoom into a small region as shown in Figs. 8(c) and (d). This can be easily recognized by observing Eq. (11) and considering the fact that $\mathbf{P}^{(\alpha\beta)}$ and $\mathbf{P}^{(\beta\alpha)}$ are simultaneously non-zero or zero at the same time depending on whether the interactions between grain α and β are kept or not.

For a given microstructure, the number of direct neighbor of a grain is independent of the size of microstructure. Given that the sparsity of the proposed models is defined by grain connectivity alone, sparsity increases as the size of the microstructure increases. For example, the above 487-grain microstructure gives sparsity of $S = 0.9764$ for the 1-layer sparse EHM and $S = 0.8906$ for the 2-layer sparse EHM. For the 938-grain microstructure (Fig. 2(h)), $S = 0.9875$ for the 1-layer sparse EHM and $S = 0.9397$ for the 2-layer sparse EHM. The increasing sparsity as a function of microstructure size indicates higher efficiency of the sparse EHM at larger microstructure sizes, which is discussed further below.

Figure 9 demonstrates the compressed row storage (CRS) format of a sparse matrix employed in this study, which significantly decreases the storage requirements proportional to the system sparsity. Figure 10 shows the reordered one-layer and two-layer sparse EHM systems for the 487-grain microstructure (Fig. 8) using the reverse Cuthill-McKee ordering and approximate minimum degree ordering schemes. While the former is intended to reduce the bandwidth of the matrix [13], the latter aims at producing factors with relatively low fill-in operations for efficient calculation [4] and is employed in the current study. Since the system sparsity structure remains unchanged throughout the multiscale analysis, the CRS format construction and reordering of the sparse linear system is performed only once at the beginning of the analysis.

Both direct and iterative solvers are available for sparse systems. For the direct sparse

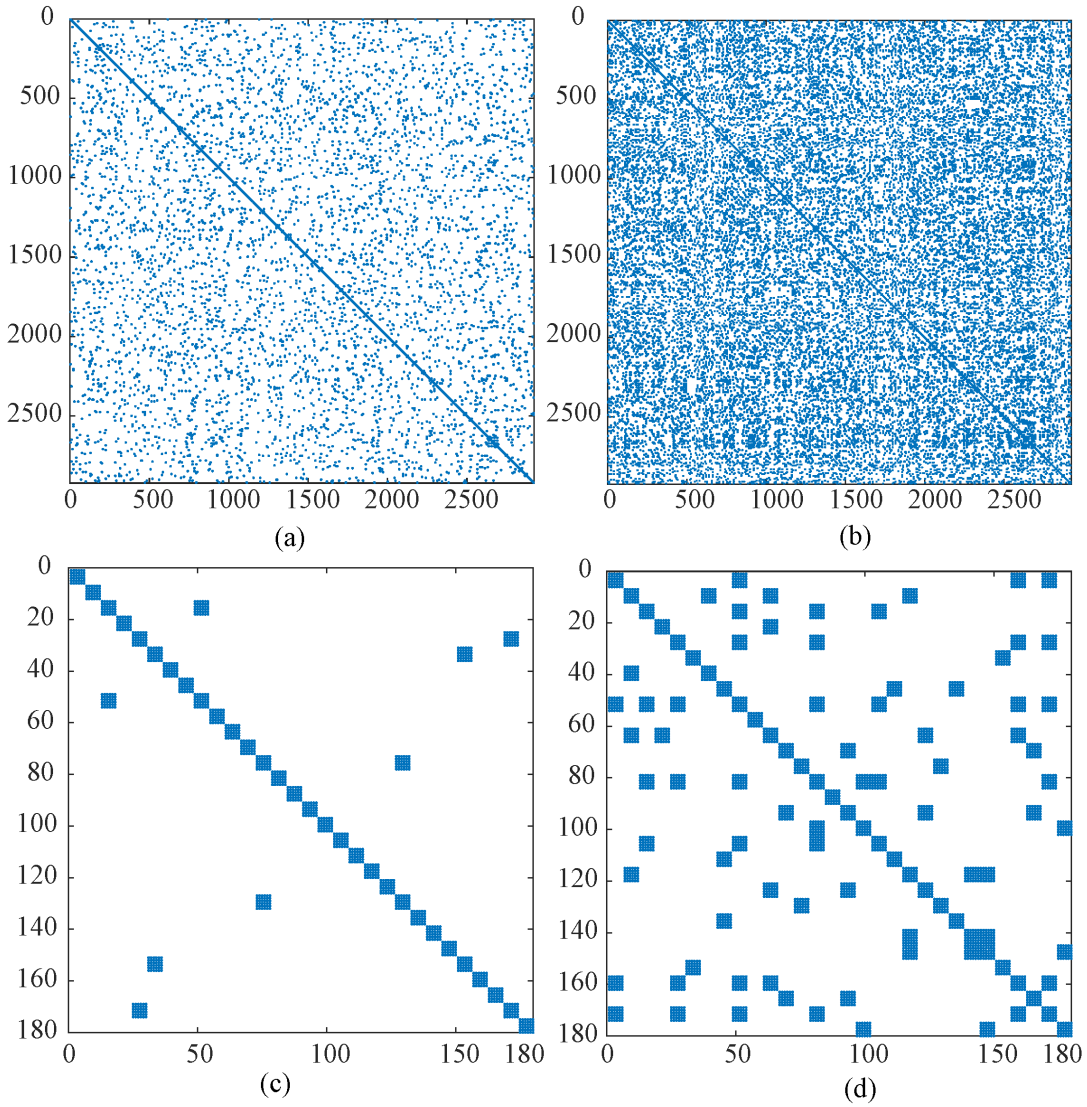

Figure 8: Structurally symmetric sparsity pattern of the linearized 487-grain EHM system: (a) one-layer clustering scheme; (b) two-layer clustering scheme; (c)-(d) zoom into the first 180x180 components of (a) and (b).

$$\mathbf{A} = \begin{bmatrix} a_{11} & a_{12} & 0 & a_{14} \\ 0 & a_{22} & a_{23} & 0 \\ a_{31} & 0 & a_{33} & a_{34} \\ a_{41} & 0 & 0 & a_{44} \end{bmatrix} CRS \begin{cases} Column\ index: & ja(nnz) = & 1 & 2 & 4 & 2 & 3 & 1 & 3 & 4 & 1 & 4 \\ Values: & a(nnz) = & a_{11} & a_{12} & a_{14} & a_{22} & a_{23} & a_{31} & a_{33} & a_{34} & a_{41} & a_{44} \\ Row\ pointer: & ia(N+1) = & 1 & 4 & 6 & 9 & 11 & & & & & \\ & N = 4 & nnz = 10 & & & & & & & & & \end{cases}$$

Figure 9: Illustration of the CRS format of a sparse matrix.

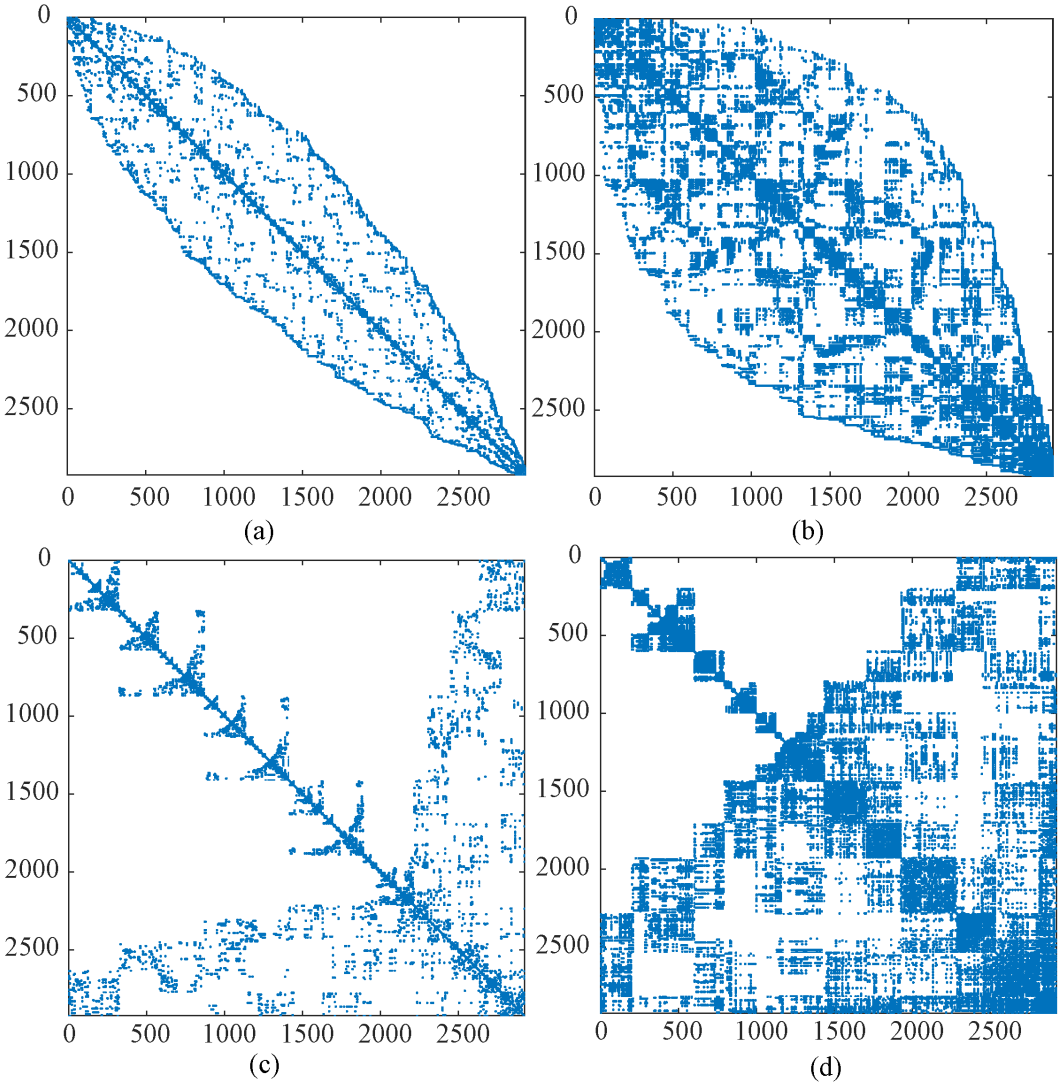

Figure 10: Reordering of the sparse EHM system: (a)-(b) reverse Cuthill-Mckee ordering of the one-layer and two-layer sparse EHM system; (c)-(d) approximate minimum degree ordering of the one-layer and two-layer sparse EHM system.

solver, PARDISO ([43, 42]) is used. PARDISO stands for Parallel Sparse Direct Solver and is an LU decomposition-based high-performance linear solver for solving large sparse linear system of equations. PARDISO splits the solving process into four sequential tasks: analysis and symbolic factorization, numerical factorization, forward and backward substitution and a final termination to release all internal solver memory. These four separate procedures allow the flexibility to conduct certain operations only once and to be used multiple times later on as discussed next since the sparsity pattern of the linear system remains unchanged throughout the macroscale analysis. For the iterative solver, we use FGMRES and GS preconditioning as discussed in Section 2. While direct sparse solvers can save some operations when solving different systems (e.g., linear system from different N-R iterations) with the same sparsity pattern, iterative sparse solvers could not. This requires different treatment when embedding the direct and iterative sparse solvers into EHM for maximum efficiency. Since the focus in this manuscript is to introduce and leverage the sparsity, we do not employ the parallelism in either solvers and only use them as serial solvers.

4.2 Efficient embedding of direct sparse solver into EHM

Figure 11 shows the implementation strategy for the sparse EHM approach using the sparse linear solvers discussed above. The implementation is performed in two stages (1) preprocessing; and (2) multiscale analysis. In the preprocessing stage, the grain clustering procedure is conducted on the microstructure to identify the grain cluster, Ω_{nc}^{α}, for each grain. The lumping procedures elaborated in Section 3 are performed for each grain to obtain the coefficient tensors for the sparse EHM. The grain clustering information is further utilized to identify sparsity pattern of the linear system and construct the CRS.

At the onset of the multiscale analysis, all material data is read and the sparse solver is initialized. At each integration point of each increment of the multiscale analysis, the reduced order system is solved using the N-R procedure and the tangent moduli is calculated (right dashed box in Fig. 11). At the end of the multiscale analysis, the sparse solver is terminated.

When initializing the sparse solver, the sparsity pattern of the system is used to identify the positions of non-zero blocks of the linear system and to conduct the reordering of the system. In the case of direct solver, symbolic factorization is also conducted once since it only depends on the sparsity pattern. At each N-R iteration (right dashed box in Fig. 11), only non-zero blocks of the Jacobian (Eq. (10)) are calculated to directly feed the CRS, and passed to the linear solver. While the number of FLOPs for constructing a full EHM system scales with $(6n)^2$, the number of FLOPs for constructing a sparse EHM system scales with $(6n)^2 * (1 - S)$.

In the case of direct solver, only numerical factorization and back substitutions are needed to solve the system at each iteration, allowing computational cost savings on the analysis, reordering and symbolic factorization. The number of FLOPs needed for numerical factorization and back substitution in the full EHM is $O((6n)^3)$. Number of FLOPs needed for the same operations on the sparse EHM, while dependent on the level and pattern of sparsity, is

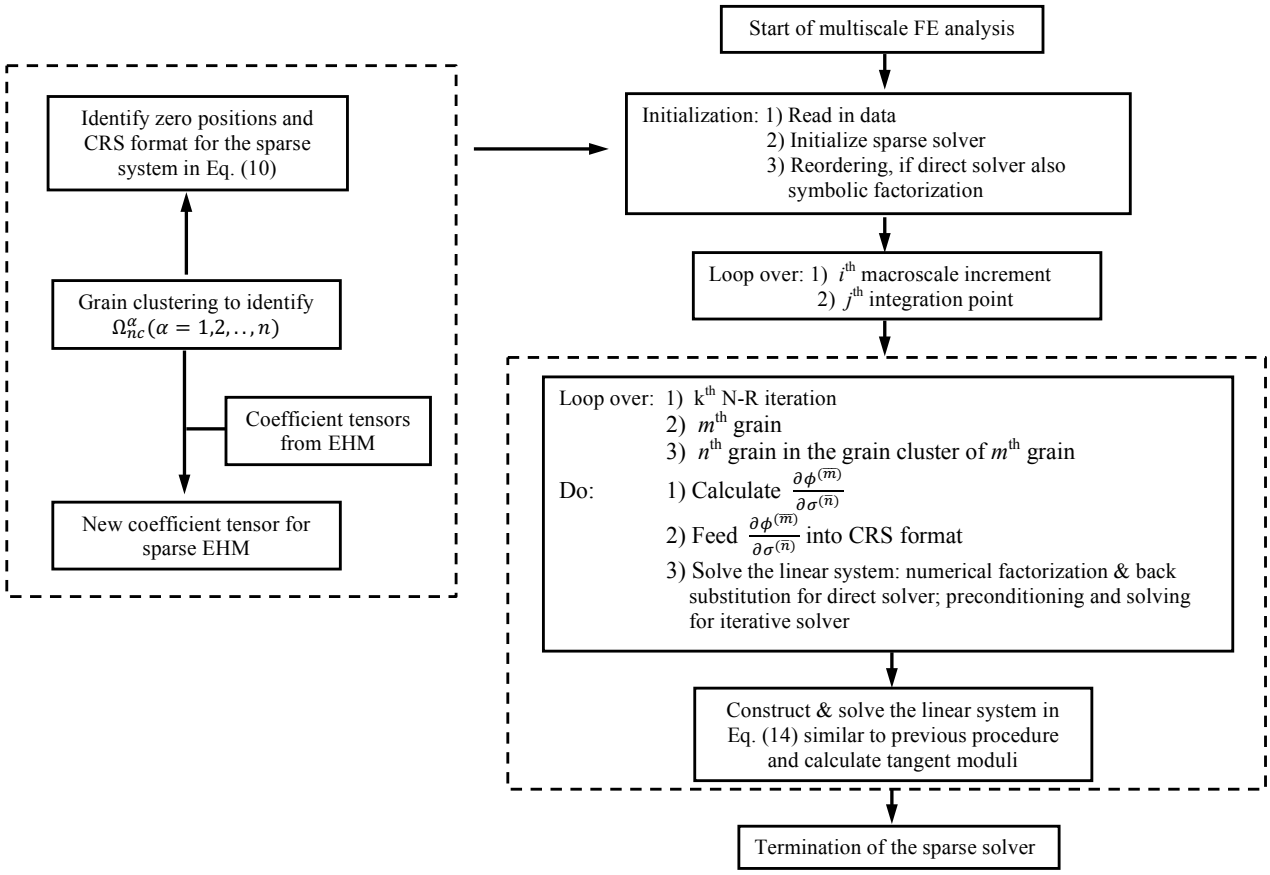

Figure 11: Schematic demonstration of the embedding of the sparse solver: left, preprocessing and right, multiscale analysis.

typically far less than $O((6n)^3)$. In the case of iterative solver, a complete preconditioning and solving is necessary for each N-R iteration to obtain the solution. While it is generally difficult to theoretically estimate the number of FLOPs of an iterative solver, system sparsity contributes to the overall efficiency as demonstrated by the numerical examples below.

Upon convergence, a similar procedure is taken to evaluate Eq. (14) for the tangent moduli calculation. Although Eq. (14) has six right-hand side vectors, one numerical factorization (major computation cost) and six back-substitutions (minor computation cost) are performed in the direct solver. In the case of iterative solver, computational cost is directly proportional to the number of right-hand side vectors.

5 Numerical verification

The verification of the sparse reduced order homogenization based crystal plasticity model is performed using two sets of examples. The examples aim at probing the accuracy and efficiency characteristics of the proposed sparse EHM models as compared with CPFE as well as full EHM. The first set of examples compare different sparse EHM models (one-layer and two-layer, strain compatibility or simultaneous iso-stress/strain constrained) with CPFE and full EHM on single phase polycrystal microstructures. While the accuracy of different sparse EHM models are evaluated in terms of overall stress-strain response and local stress distributions, we particularly focus on the assessment of efficiency of the proposed models. The second set of examples evaluate the performance of sparse EHM on two-phase polycrystal microstructures in order to quantify accuracy in the presence of high phase property contrast. A multiscale example is also provided to demonstrate the capability of sparse EHM in solving a large polycrystalline structure.

5.1 Single phase polycrystals

The material considered is pure aluminum which has FCC lattice and 12 $\{111\}\langle 111\rangle$ slip systems. The elastic parameters are $C_{11} = 108.2$ GPa, $C_{12} = 61.3$ GPa, $C_{44} = 28.5$ GPa, while the remainder of the inelastic parameters are listed in Table 3. The RVE is taken to consist of 487 grains and the microstructure is shown in Fig. 2(f). The microstructure is loaded uniaxially along X direction up to 5% strain at strain rate of 0.05/s. The finite element discretization of the reference CPFE model is composed of 176,415 trilinear four-noded tetrahedron elements with 31,777 nodes, resulting in a system with 95,331 DOF. The CPFE models with tri-linear tetrahedral elements are known to exhibit some volumetric locking [11]. The CPFE simulations were checked for the existence of checkerboard patterning in the pressure contours [1]. The checkerboard patterning was observed to be very small indicating a minor effect of volumetric locking. The partitioning of the proposed reduced order models were performed such that each part coincides with a single grain (i.e., n= 487) leading to a nonlinear system with 2,922 degrees of freedom. The macroscale discretization of the multiscale model consists of a single tri-linear eight-noded hexahedron element.

Table 3: Inelastic parameters [31].

m	$\dot{\gamma}_0(s^{-1})$	h_0 (MPa)	g_0^s (MPa)	$g_{sa,0}^s$ (MPa)	m'	$\dot{\gamma}_{s0}(s^{-1})$
0.05	1.0	20.4	3.7	30.8	0.0	5.0×10^{10}

The overall stress-strain response obtained by the CPFE, full EHM and the ϵ-EHM models are shown in Fig. 12(a), in which -1 and -2 indicates the 1-layer and 2-layer sparse EHM, respectively. The comparison between CPFE, full EHM and σ-EHM models are shown in Fig. 12(b). Under the uniaxial loading, both ϵ-EHM and σ-EHM models provide almost identical results to the full EHM model, indicating the relative insignificance of the grain interactions on the overall response in this example. The discrepancy between the EHM and CPFE models is about 3% at the end of the simulation. The normalized stress distributions at the grain-scale, computed with the CPFE and the EHM models are shown in Fig. 13. The normalized stress refers to the Von Mises stress within a grain normalized with the initial strength, g_0 in Fig. 13(a,b). Similarly, the normalized stresses transverse to the loading direction (σ_{22}/g_0) are compared in Fig. 13(c,d). The figures display the volume fraction of grains within the microstructure as a function of the normalized stress experienced by the grains, in the form of a histogram. For clarity, the bin plot representation is included only for the CPFE model. The data points on the line plots for the EHM models refer to the mid-point of the stress range associated with each bin of the histogram plot. The ϵ-EHM-0 is identical to the Taylor model as stated in Remark 2. The local normalized stress distributions predicted by ϵ-EHM-0 have a larger error compared to the other EHM models, especially in the transverse direction. The stress distributions for the remainder of the EHM models match the CPFE results with reasonable accuracy. While the Von-Mises stresses for the ϵ-EHM-1,2 and σ-EHM-1,2 models are very similar, transverse stresses indicate some variation with slightly better accuracy in the σ-EHM models. The accuracy of the EHM models in capturing the local stress distributions could be further improved by increasing the reduced model order by partitioning the grains with more than a single part as discussed in Ref. [60].

We also compared the response of different EHM models and the CPFE model under simple shear loading up to 5% strain loaded at a strain rate of 0.05/s. The overall stress-strain responses are shown in Fig. 14(a) and the local responses are shown in Fig. 14(b). The behavior and accuracy characteristics of the EHM models are similar to the cases discussed above. For the overall response, the discrepancy between the stress magnitudes computed by the full EHM and the CPFE models at the end of the simulation is approximately 2.5%, while ϵ-EHM-1 and ϵ-EHM-2 results show a discrepancy of 2.7% compared with the CPFE results.

The efficiency characteristics of the EHM models are assessed by performing simulations with varying microstructural complexity (parameterized by the RVE size) as shown in Fig. 2(b)-(h). The speedup of different EHM models compared with CPFE are listed in Table 4 and plotted in Fig. 15. One-layer sparse EHM models (i.e., ϵ-EHM-1 and σ-EHM-1) provide significant speedup compared with full EHM and a much slower efficiency degradation as the

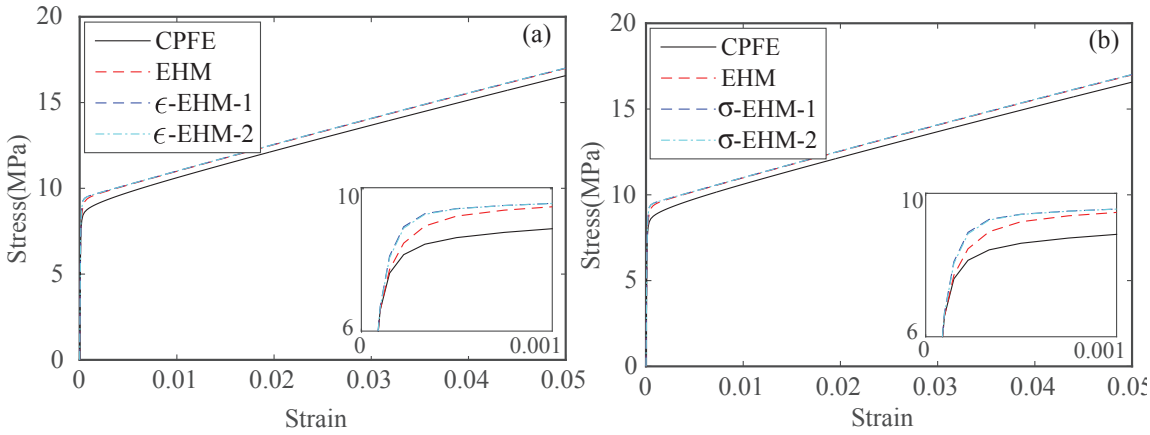

Figure 12: Overall stress-strain response comparison between CPFE, EHM and: (a) ϵ-EHMs; (b) σ-EHMs.

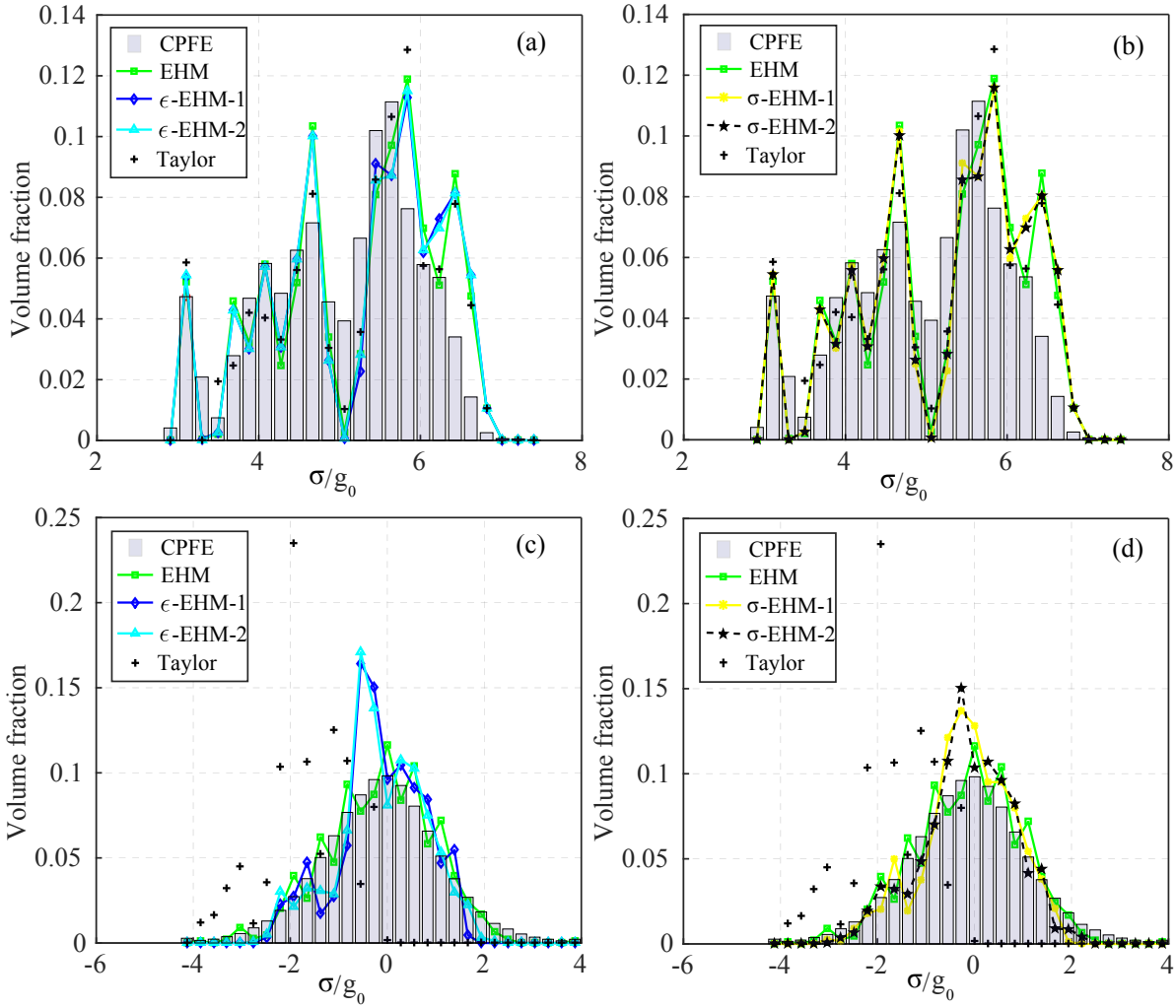

Figure 13: Local normalized stress distribution: (a)-(b) Von Mises stress; (c)-(d) stress component σ_{22}.

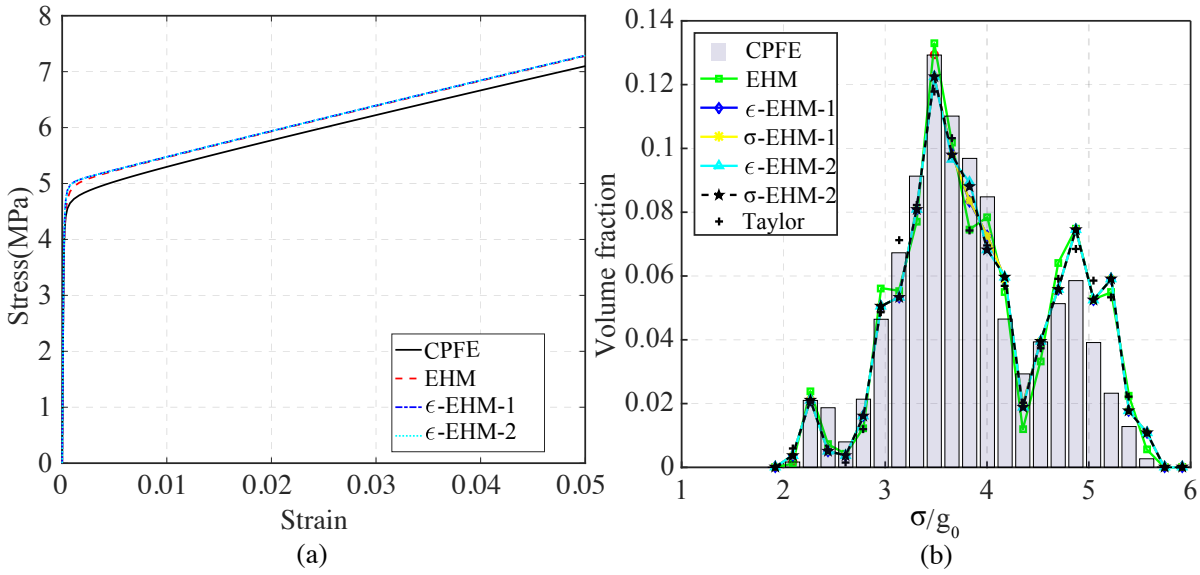

Figure 14: The 487-grain under simple shear: (a) Overall stress strain response; (b) Normalized Von Mises stress distribution.

Table 4: Speedup of EHM and sparse EHM models compared with CPFE.

n	R_{EHM}	$R_{\epsilon\text{-EHM-1}}$	$R_{\sigma\text{-EHM-1}}$	$R_{\epsilon\text{-EHM-2}}$	$R_{\sigma\text{-EHM-2}}$
85	111.74	279.35	258.96	120.13	118.46
154	53.89	200.20	197.26	68.40	67.45
242	26.61	164.51	166.06	64.66	64.50
347	15.66	116.05	113.69	45.11	43.92
487	8.38	85.08	83.72	34.96	34.55
629	5.66	70.24	68.22	26.11	25.67
938	2.62	48.15	48.36	14.31	14.72

microstructure size increases. From the 85-grain to the 938-grain RVE, speedup of full EHM reduces by a factor of 44.1, while the ϵ-EHM-1 only reduces by a factor of 5.8 and theϵ-EHM-2 reduces by a factor of 8.4. For a 938-grain microstructure, the one-layer sparse EHM models provide speedup of 48 compared with the direct CPFE simulation.

To investigate the effect of sparsity, we compare the efficiency of different sparse EHM compared with the full EHMs. To ensure a fair comparison between full EHM and different sparse EHM models, we first confirmed that all models compared have similar number of load increments and iterations at the micro- and macroscopic scales. All analyses consist of approximately 122 load increments, and 246 macroscale iterations, resulting in a total of 2050 microscale iterations. The fluctuations in number of iterations in different models are within 5% compared with the above values. The speedup of sparse EHMs compared with the full EHM (defined by the ratio between simulation time of full EHM and sparse EHM models) are plotted in Fig. 15(b), together with the speedup of linear solver portion (accumulated CPU

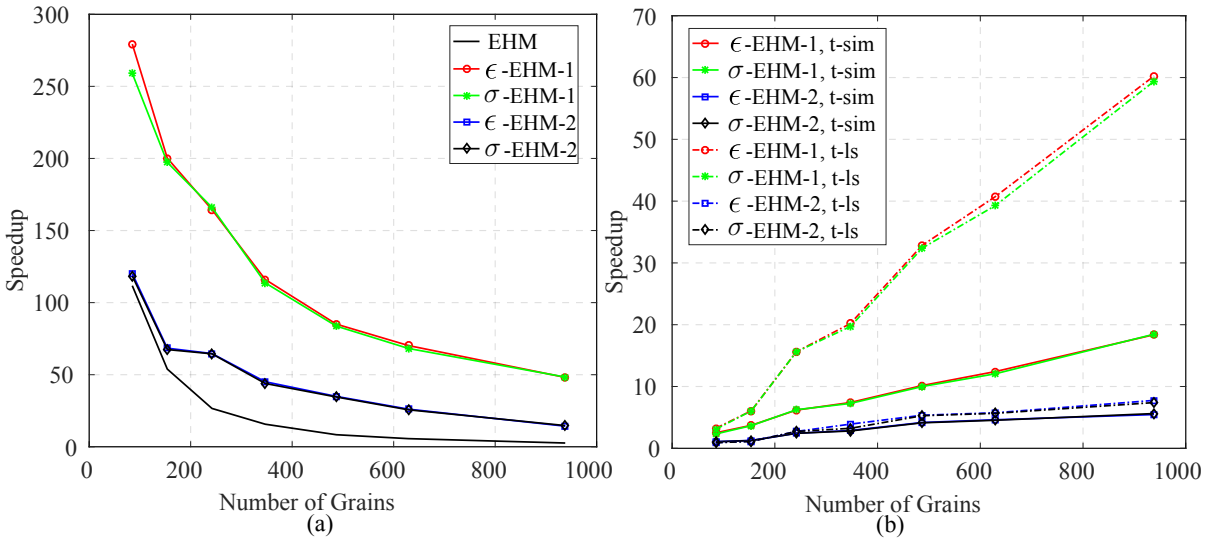

Figure 15: Speedup of: (a) EHM and sparse EHM models compared with the CPFE model; (b) sparse EHM models compared with the full EHM model.

time spent for linear solver in N-R iterations). It is observed that the speedup of one-layer sparse EHM compared with full EHM increases linearly as the number of grains increases. The speedup of the two-layer sparse EHM compared with EHM, shows a sub-linear relationship with number of grains. This is because sparsity decreases fast from the one-layer sparse EHM to the two-layer sparse EHM, and the FLOPs for solving a sparse linear system increase fast with decrease in sparsity. The behavior of speedup for the linear solver portion is generally similar to the total simulation times, the curves display much higher slopes. This is because the other procedures (i.e. computation of slip and hardening evolution, matrix constructions etc.) are of similar order for all models, including the full EHM and sparse EHM.

Figure 15 shows the efficiency of ϵ-EHM-1 using the iterative solver as a function of RVE size. It clearly shows that sparsity also significantly increases the efficiency of EHM when using the iterative solver, while the speedup is less than that of direct solver in the cases we studied. For both direct and iterative solvers, the sparse EHM scales larger than $O(n)$ observed in the CPFE model. This implies that there may exist a trade-off point, for which the sparse EHM model performance could degrade below the performance of the CPFE model. However, the number of grains to reach this trade-off point is beyond microstructure sizes typically needed to define a representative volume.

5.2 Two-phase polycrystals

The accuracy characteristics of the reduced order microstructure models degrade as a function of the property contrast between constituents. For example, Taylor's hypothesis generally performs well in single-phase materials exhibiting moderate crystal anisotropy, but yields too stiff response for multiphase materials with higher anisotropy or hexagonal symmetry [28]. In

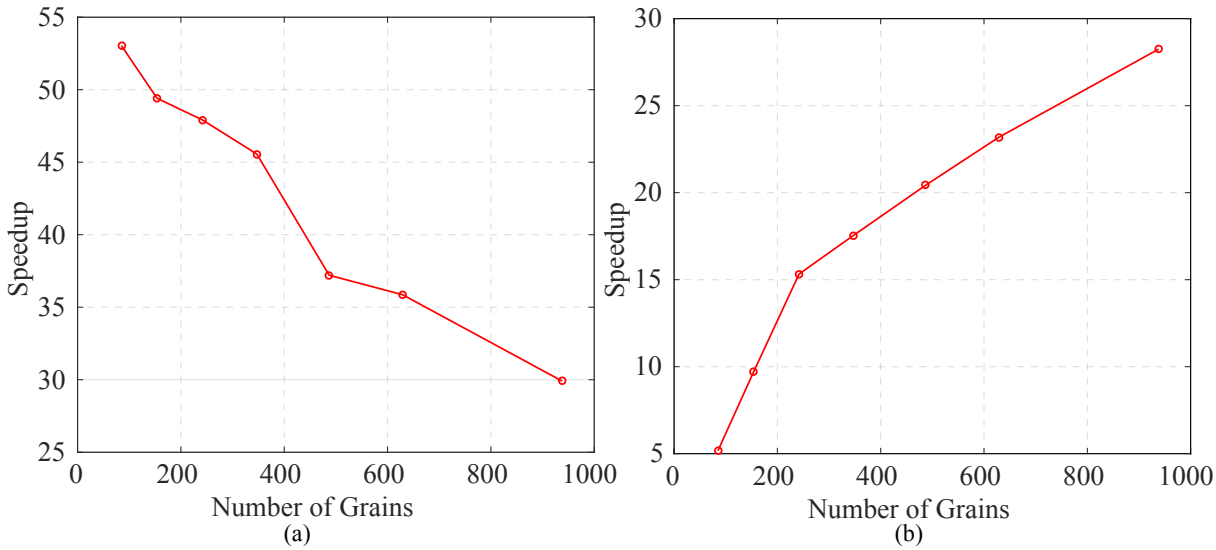

Figure 16: Speedup of ϵ-EHM-1 using iterative solver compared with: (a) CPFE model and (b) full EHM model using iterative solver.

single phase materials such as discussed in the above example, the material property contrasts are relatively small. In the current example we consider a two-phase FCC material where the two phases have significant property contrast.

Figure 17 illustrates the morphology of the two microstructures employed in this example. The microstructures consist of 242 and 629 grains. Each grain within the microstructures is randomly assigned to one of the two phases. The volume fraction of each phase is approximately 0.5. The material parameters of the two phases are listed in Table 5. In all simulations considered below, phase 1 parameters are fixed (first row in Table 5). Two cases of simulations are considered, in which all the grains in phase 2 are assigned either the "low contrast" parameters (second row in Table 5) or the "high contrast" parameters (third row in Table 5).

To evaluate the accuracy of different sparse EHM formulations (i.e., ϵ-EHM and σ-EHM) in the two-phase polycrystal case, we first use the 242-grain microstructure as shown in Fig. 17(a). The material properties for phase two are taken to have the smaller phase contrast (row 2 of Table 5). The microstructure is loaded uniaxially along the X direction up to 5% strain at a strain rate of 0.05/s. The overall stress-strain response of the two different formulations compared with CPFE and full EHM are shown in Fig. 18, which shows increasing predicted stress from CPFE to full EHM to one-layer and two-layer sparse EHM. The discrepancies between the full EHM and the sparse EHM are more distinguishable in the two-phase microstructure, while they are nearly identical in the case of single phase polycrystals. The local response in terms of the spatial distribution of the Von Mises stress computed with, sparse EHM, CPFE and full EHM are shown in Fig. 19. The predictions from ϵ-EHM and σ-EHM are very similar and closely match those of the CPFE and full EHM. While the differences between one-layer sparse EHM and full EHM are relatively larger than that in the single phase microstructure, the differences between one-layer sparse EHM and two-layer EHM are still very small. The

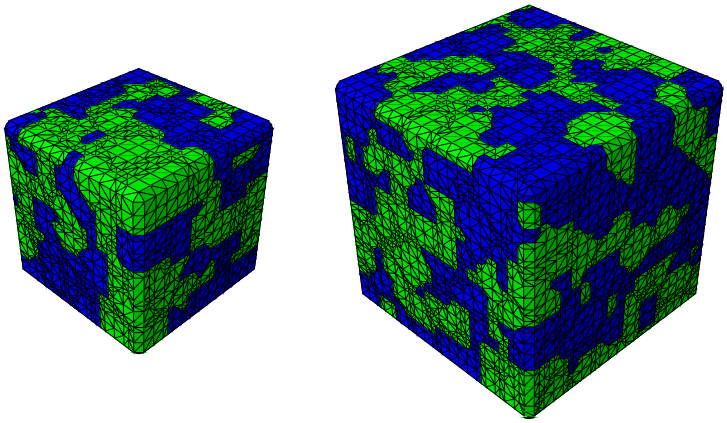

(a) (b)

Figure 17: Two-phase microstructures with: (a) 242-grain microstructure; (b) 629-grain microstructure rendered with green for phase 1 and blue for phase 2.

Table 5: Inelastic parameters for different phases.

Phase ID	m	$\dot{\gamma}_0(s^{-1})$	h_0 (MPa)	g_0^s (MPa)	$g_{sa,0}^s$ (MPa)	m'	$\dot{\gamma}_{s0}(s^{-1})$
1	0.05	1.0	20.4	3.7	30.8	0.0	5.0×10^{10}
2 (low contrast)	0.05	1.0	50.0	10.0	30.8	0.0	5.0×10^{10}
2 (high contrast)	0.05	1.0	200.0	30.0	50.0	0.0	5.0×10^{10}

full EHM, one-layer and two-layer sparse EHM all provide better local stress predictions than Taylor model compared with CPFE simulation.

The above mentioned investigation is repeated in the presence of a higher phase contrast (i.e., material properties of phase two taken to be row 3 of Table 5). The stress-strain response of the higher phase contrast case is shown in Fig. 20(a), along with the corresponding local stress distributions (Fig. 20(b)). The one-layer and two-layer sparse EHM provide almost identical results, yet the discrepancies between the sparse EHMs, full EHM and CPFE are more distinguishable. The stress level from full EHM is 6.4% higher than the CPFE, whereas one-layer and two-layer sparse EHMs are 8.3% higher than CPFE. Similar discrepancies between the sparse EHMs, full EHM and CPFE in the local stress distributions are observed. At the end of the analyses of the low contrast case shown in Fig. 18, the stress magnitude from full EHM is 2.8% higher than the CPFE, whereas one-layer and two-layer sparse EHMs are 3.6% higher than CPFE. In the higher phase contrast case shown in Fig. 20, the stress magnitude from full EHM is 5.8% higher than the CPFE, whereas one-layer and two-layer sparse EHM models are 8.3% higher than the CPFE. This comparison indicates that higher phase contrast increases the discrepancy between full EHM and CPFE as well as the discrepancy between full EHM and sparse EHMs. Increase in the property contrast has been previously shown to degrade the full EHM accuracy (Ref. [59]). The current results indicate that the accuracy of sparse EHMs also degrades compared to the full EHM as a function of property contrast. The reduction in the accuracy of sparse EHMs compared to the full EHM is attributed to

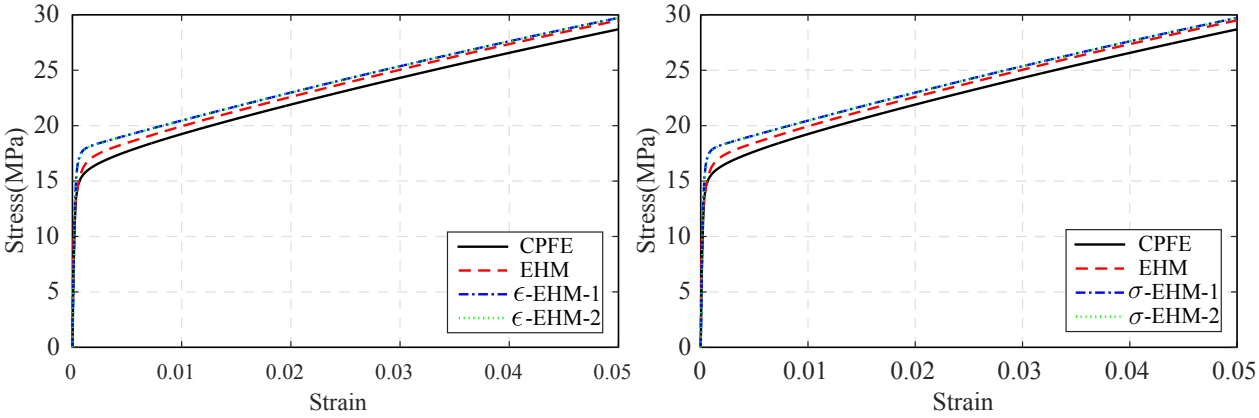

Figure 18: Overall response comparison of the low phase contrast 242-grain microstructure between CPFE, full EHM and: (a) ϵ-EHMs; (b) σ-EHMs.

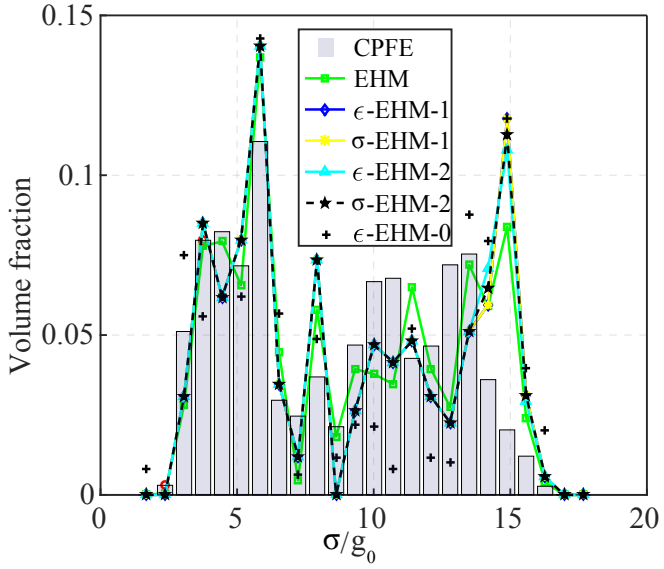

Figure 19: Von Mises stress distribution comparison of the 242-grain microstructure with low phase contrast.

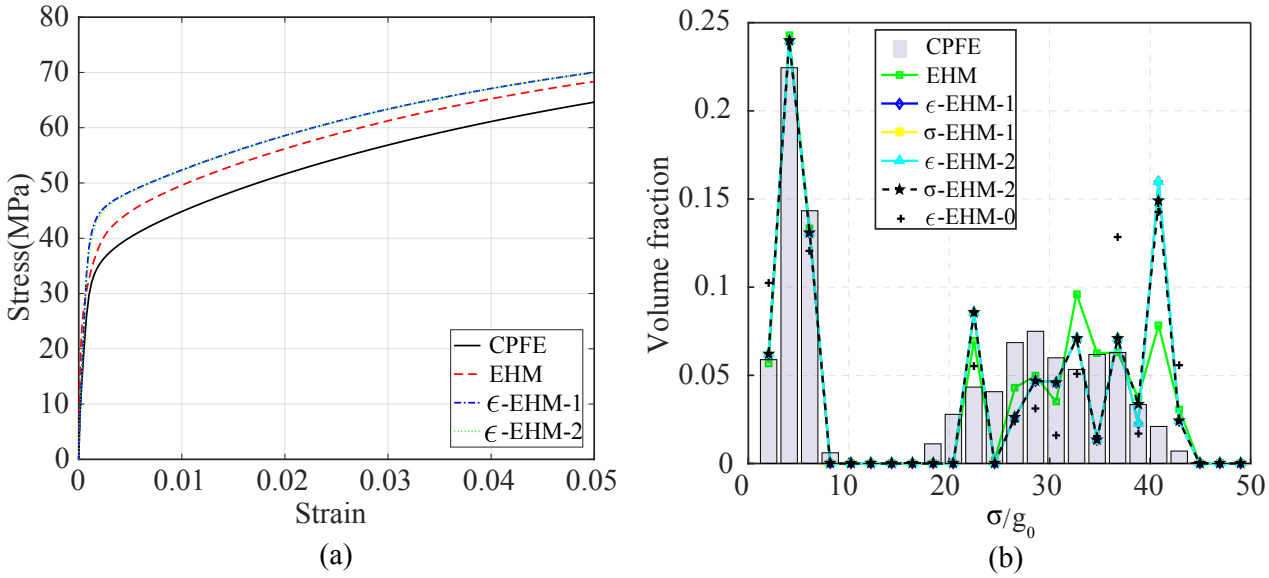

Figure 20: Response of the 242-grain microstructure with high phase contrast: (a) overall stress-strain; (b) local Von Mises stress distribution.

the increasing role of grain interactions (i.e., longer range stresses within the microstructure), which are partly neglected in the sparse EHM models.

Fig. 21 illustrates the accuracy characteristics of the proposed models under different loading conditions. We consider biaxial tension with either monotonic loading or cyclic loading conditions for the 629-grain microstructure (Fig. 17(b)) using the above higher contrast two-phase material. The figure shows the overall stress-strain response along the X and Y directions. For the biaxial monotonic tension with proportional loading, 5% strain is applied along the X direction with a strain rate of 0.005/s, while a 3% strain is applied along the Y direction with a strain rate 0.003/s (Fig. 21(a,b)). Compared with the CPFE, the full EHM exhibits errors of 9.36% and 14.13% at 1% strain for X and Y directions, respectively. ϵ-EHM-1 and ϵ-EHM-2 show similar accuracy with the full EHM with 11.01% and 15.06% error. At the end of the simulation, the full EHM as well as the sparse EHM models display stress errors less than 1% and 6.5% along the X and Y directions, respectively. For the non-proportional biaxial loading case, 6% maximum strain is applied along the X direction with a constant strain rate of 0.04/s. Upon reaching the maximum strain, the loading is held constant at 6% until the end of the simulation. Along the Y direction, the microstructure is cyclically loaded with an R-ratio of -1 and applied strain range of 4% at constant strain rate 0.04/s (Fig. 21(c,d)). The duration of the cyclic biaxial tension simulation is 2.5 s. Compared with the CPFE, the full EHM exhibits errors of 9.61% and 14.29% at 1% strain for X and Y directions, respectively. ϵ-EHM-1 and ϵ-EHM-2 show similar accuracy with the full EHM with 10.76% and 15.66% error. At the end of simulation, the full EHM as well as the sparse EHM models display stress errors less than 6.5% and 6.9% along the X and Y directions, respectively.

While some discrepancy between the CPFE and the EHM models exists, the errors intro-

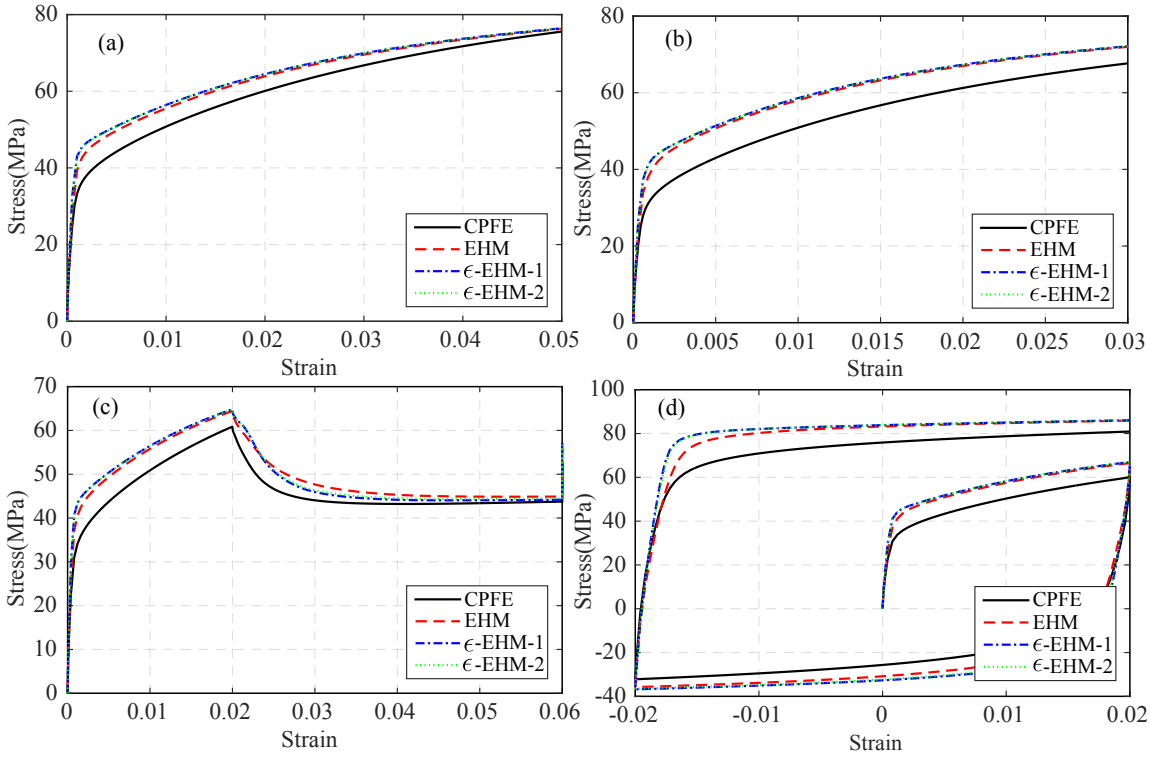

Figure 21: Stress-strain response of: (a) proportional biaxial loading, X direction; (b) proportional biaxial loading, Y direction; (c) non-proportional biaxial loading, X direction; (d) non-proportional biaxial loading, Y direction.

duced by the proposed sparse formulation are small. The accuracy characteristics of the full EHM method compared to the CPFE has been presented in Ref. [60]. Additional assessment of accuracy in the context of damage mechanics has been provided in Refs. [39, 57, 56, 21, 12, 58].

5.3 A macroscale example: plate with hole under bolt pressure

To demonstrate the capability of the sparse EHM in solving structural scale problems, we investigated the response of a thick plate subjected to bolt pressure. The geometry and dimensions of the plate are shown in Fig. 22. The bold load is applied as tractions at the inner surface of the hole with a spatially varying form [9]:

$$\mathbf{T}_i = -\frac{4P}{\pi D}\mathbf{n}_i \cos\theta \tag{53}$$

in which, D is the diameter of the hole (50 mm), $\mathbf{T}_i$ denotes the traction distribution inside the hole at point i, which is characterized by angle θ that measure clockwise from point A as shown in Fig. 22(b); $\mathbf{n}_i$ is the unit normal of the hole surface at point i; and P=350 N/mm.

Half of the plate is discretized due to symmetry with 27,680 tri-linear eight-noded hexa-

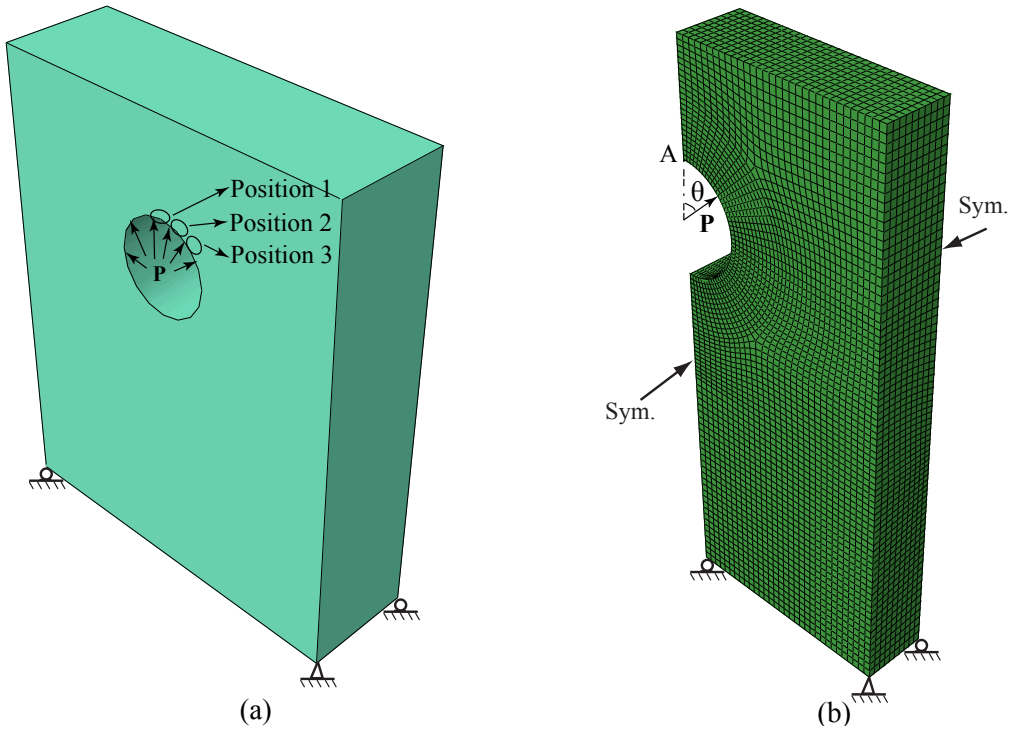

Figure 22: A plate under bolt pressure: (a) geometry and loading conditions of the plate; (b) finite element mesh.

hedron elements as shown in Fig. 22(b). The microstructure is the 938-grain RVE as shown in Fig. 2 (h). The simulation therefore tracks 25,963,840 grains throughout the domain of the specimen. Clearly, such a simulation is computationally prohibitive using the direct CPFE simulation and the classical computational homogenization. The full EHM is also expensive due to the size of the system associated with the model. In this study, the one-layer ϵ-EHM and zero-layer ϵ-EHM (i.e., Taylor model) are used to model the response of the plate.

The stress-contours of the plate at the end of loading using the zero- and one-layer ϵ-EHM are shown in Fig. 23. The macroscopic stresses are close between the two models. The overall bearing force versus the displacement at the far end of the hole (point A) predicted using the two models are identical and shown in Fig. 24. Plastic deformations near stress concentration around the hole are responsible for the nonlinearity in the force-displacement behavior.

To better understand the microscale stress variations at the grain level, three different positions around the hole are probed as shown in Fig. 22(a). 12 elements at each position are selected (probing $938 \times 12 = 11,256$ grains at each position), and the normalized Von Mises stress distributions of the microscale grains at each position are plotted in Fig. 25 at the middle and end of the simulation, respectively. The figures clearly show an increase in the local stress as deformation continues. Microscale stress histograms also show a decreasing grain level Von Mises stress from position 1, 2 to 3, which is in accordance with the macroscale stress at position 1, 2 and 3 as shown in Fig. 22. In contrast to the global behavior, the ϵ-EHM-0 and ϵ-EHM-1 models demonstrate variations in local stresses as shown in Figs. 23 and 24. The

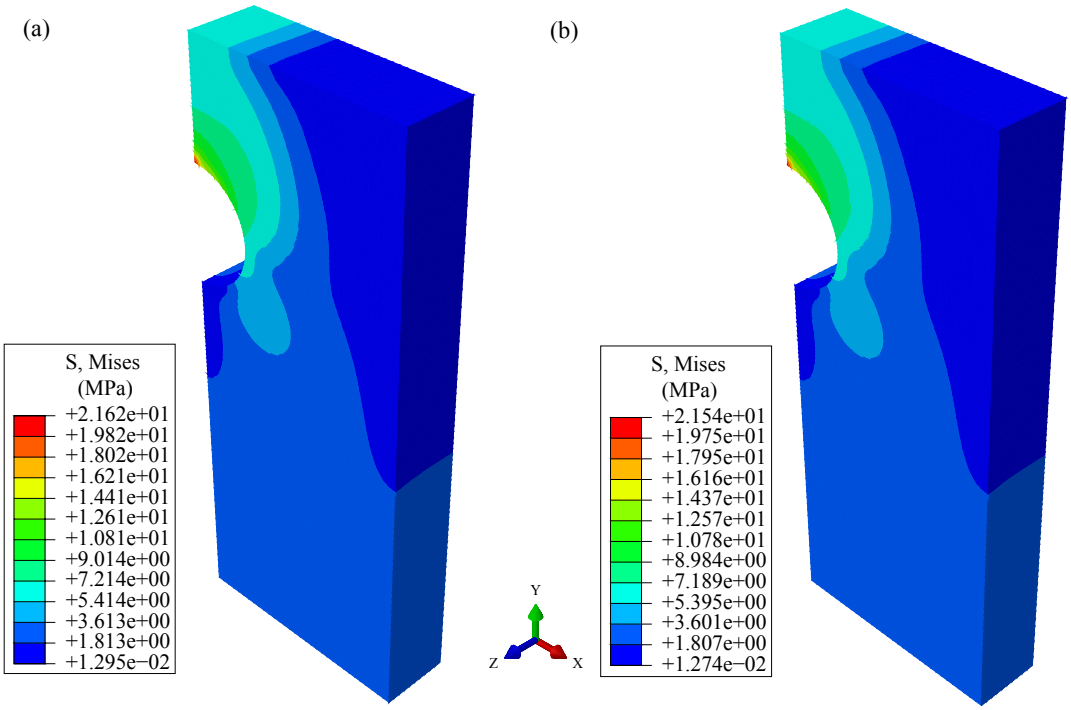

Figure 23: Von Mises stress contour at the end of simulation: (a) ϵ-EHM-1 model; (b) ϵ-EHM-0 model.

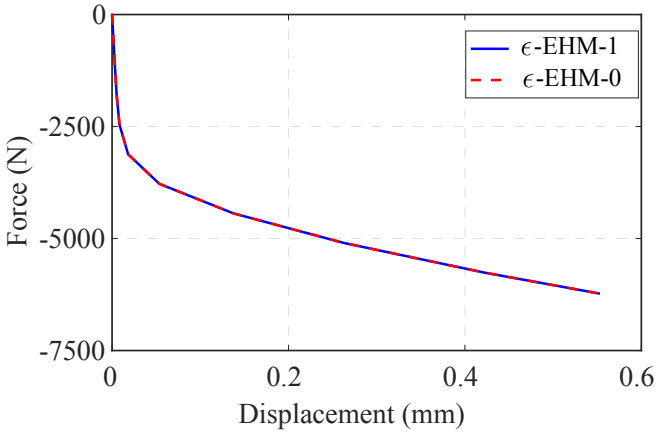

Figure 24: Bearing force-displacement curve of the plate.

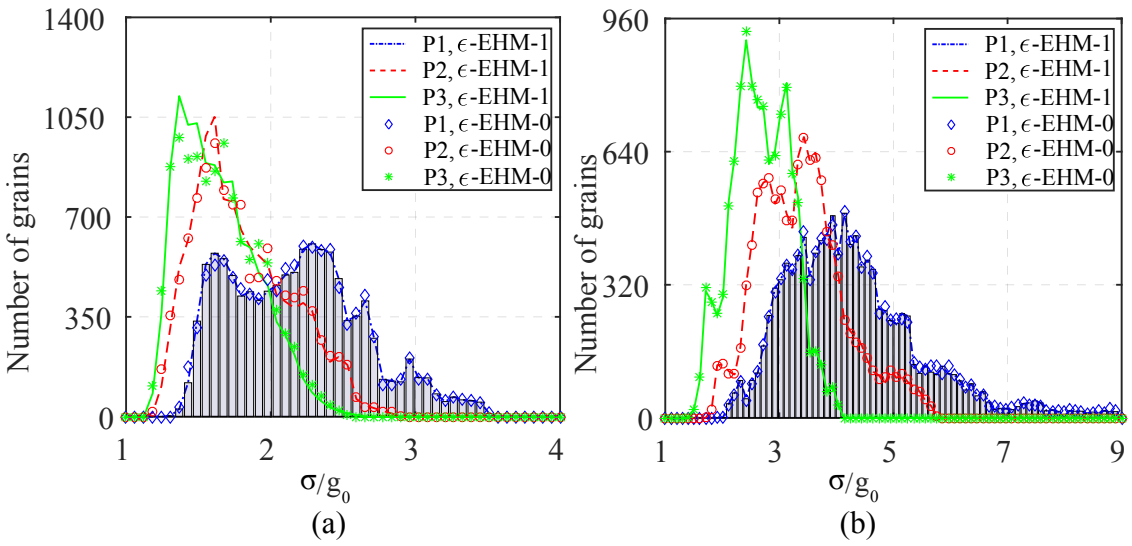

Figure 25: Normalized Von Mises stress histogram of the three positions at: (a) middle; (b) end of the simulation.

variations are relatively more significant during the elastic-plastic transition. Once most of the grains within the localized regions start to undergo fully plastic deformations, the variations between the two models decrease in magnitude.

6 Conclusions and Future Research Interests

We presented a grain-cluster accelerated eigenstrain-based reduced-order homogenization model for computationally efficient modeling of complex polycrystal microstructures. The efficiency gain is obtained through introducing sparsity into the linear system associated with full EHM formulation by selectively considering grain-to-grain interactions. A neighborhood-based grain-clustering scheme is developed to consistently identify grain neighborhoods for each grain, between which interactions are considered. This manuscript introduced a hierarchy of reduced models that recovers eigenstrain-based homogenization when full range of interactions are considered. The proposed sparse EHM maintains high efficiency as the RVE size increases with negligible reduction in accuracy compared to the full EHM approach. The proposed sparse EHM models open the possibility of performing relatively large scale structural simulations, in which the grain level information can be directly tracked throughout the structural domain and throughout the duration of a structural analysis. The future work will focus on analysis of structural components subjected to extreme loading and environments, which requires the extension of the proposed model to (a) address thermo-mechanical behavior, and (b) incorporate HCP grains for applicability to a wider range of materials.

7 Acknowledgement

The authors gratefully acknowledge the research funding from the Air Force Office of Science Research Multi-Scale Structural Mechanics and Prognosis Program (Grant No: FA9550-13-1-0104. Program Manager: Dr. Jaimie Tiley). We also acknowledge the technical cooperation of the Structural Science Center of the Air Force Research Laboratory.

Appendix

The coefficient tensors $\mathbf{A}$ and $\mathbf{P}$ are functions of elastic ($\mathbf{H}(\mathbf{y})$) and phase inelastic ($\mathbf{h}^{(\alpha)}(\mathbf{y})$) influence functions. The expressions for the coefficient tensors are:

$$A^{(\beta)}_{ijkl} = I_{ijkl} + \int_{\Theta^{(\beta)}} H_{(i,y_j),kl}(\mathbf{y})\big)\,\mathrm{d}\mathbf{y} \tag{54}$$

$$P^{(\beta\alpha)}_{ijkl} = \frac{1}{|\Theta^{(\beta)}|}\int_{\Theta^{(\beta)}}\int_{\Theta^{(\alpha)}} h_{(i,y_j)kl}(\mathbf{y},\hat{\mathbf{y}})\,\mathrm{d}\hat{\mathbf{y}}\,\mathrm{d}\mathbf{y} \tag{55}$$

$$M^{(\alpha)}_{ijkl} = \frac{1}{|\Theta^{\alpha}|}\int_{\Theta^{(\alpha)}} M_{ijkl}(\mathbf{y})\,\mathrm{d}\mathbf{y} \tag{56}$$

where $\mathbf{I}$ is the identity tensor, $\mathbf{M}$ the compliance tensor. Elastic and phase inelastic influence functions, $\mathbf{H}(\mathbf{y})$ and $\mathbf{h}(\mathbf{y})$, are calculated from the so called elastic influence function problem and phase inelastic influence function problem given in Box 1 and 2. Inspecting the expression for $\mathbf{P}^{(\alpha,\beta)}$ in Eq. (55, one can find:

$$c^{(\bar{\beta})}\mathbf{P}^{(\bar{\beta}\bar{\alpha})} = c^{(\bar{\alpha})}\mathbf{P}^{(\bar{\alpha}\bar{\beta})} \tag{57}$$

$$\{L_{ijmn}(\mathbf{y})[H_{(m,y_n)kl}(\mathbf{y}) + I_{mnkl}]\}_{,y_j} = 0; \qquad \mathbf{y}\in\Theta$$
$$\Theta - \text{periodic boundary conditions on } \mathbf{y}\in\Gamma_\Theta$$

Box 1: Elastic influence function problem.

$$\Big\{L_{ijmn}(\mathbf{y})\Big[h_{(m,y_n)kl}(\mathbf{y},\hat{\mathbf{y}}) - I_{mnkl}\,\mathrm{d}(\mathbf{y}-\hat{\mathbf{y}})\Big]\Big\}_{,y_j} = 0; \quad \mathbf{y},\hat{\mathbf{y}}\in\Theta$$
$$\Theta - \text{periodic boundary conditions on } \mathbf{y}\in\Gamma_\Theta$$
$$\mathrm{d} - \text{ the Dirac delta function}$$

Box 2: Phase inelastic influence function problem.

References

[1] ABAQUS Documentation. Dassault Systemes, Providence, RI, USA.

[2] *Intel(R) Math Kernel Library 11.3.2 Update 1 for Linux*. Intel, MKL 2016 edition, 2015.

[3] S. Ahzi A. Molinari, G.R. Canova. A self consistent approach of the large deformation polycrystal viscoplasticity. *Acta Metall.*, 35:2983–2994, 1987.

[4] P. R. Amestoy, T. A. Davis, and I. S. Duff. An approximate minimum degree ordering algorithm. *SIAM J. Matrix Anal. Appl.*, 17:886–905, 1996.

[5] M. Anahid, M. K. Samal, and S. Ghosh. Dwell fatigue crack nucleation model based on crystal plasticity finite element simulations of polycrystalline titanium alloys. *J. Mech. Phys. Solids*, 59:2157–2176, 2011.

[6] L. Anand. Constitutive equations for the rate-dependent deformation of metals at elevated temperatures. *J. Eng. Mater. Technol.*, 104:12–17, 1982.

[7] E. Anderson, Z. Bai, C. Bischof, S. Blackford, J. Demmel, J. Dongarra, J. Du Croz, A. Greenbaum, S. Hammarling, A. McKenney, and D. Sorensen. *LAPACK Users' Guide*. Society for Industrial and Applied Mathematics, Philadelphia, PA, third edition, 1999.

[8] M. Bogdanor, C. Oskay, and S. Clay. Multiscale modeling of failure in composites under model parameter uncertainty. *Comput. Mech.*, 56:389–404, 2015.

[9] F.-K. Chang and R. Scott. Strength of mechanically fastened composite joints. *J. Compos. Mater.*, 16:470–494, 1982.

[10] J. Cheng and S. Ghosh. A crystal plasticity FE model for deformation with twin nucleation in magnesium alloys. *Int. J. Plast.*, 67:148–170, 2015.

[11] J. Cheng, A. Shahba, and S. Ghosh. Stabilized tetrahedral elements for crystal plasticity finite element analysis overcoming volumetric locking. *Comput. Mech.*, 57:733–753, 2016.

[12] R. D. Crouch, S. B. Clay, and C. Oskay. Experimental and computational investigation of progressive damage accumulation in CFRP composites. *Composites Part B: Engineering*, 48:59–67, 2013.

[13] E. Cuthill and J. McKee. Reducing the bandwidth of sparse symmetric matrices. In *In Proceedings of the 1969 ACM 24th national conference*, pages 157–172. ACM, 1969.

[14] G. J. Dvorak. Transformation field analysis of inelastic composite materials. *Proc. Math. Phys. Eng. Sci.*, 437:311–327, 1992.

[15] G. J. Dvorak and Y. Benveniste. On transformation strains and uniform fields in multiphase elastic media. *Proc. Math. Phys. Eng. Sci.*, 437:291–310, 1992.

[16] P. Eisenlohr, M. Diehl, R.A. Lebensohn, and F. Roters. A spectral method solution to crystal elasto-viscoplasticity at finite strains. *Int. J. Plast.*, 46:37–53, 2013.

[17] F. Feyel and J.-L. Chaboche. FE2 multiscale approach for modelling the elastoviscoplastic behaviour of long fibre SiC/Ti composite materials. *Comput. Methods Appl. Mech. Engrg.*, 183:309–330, 2000.

[18] R. Hill. Elastic properties of reinforced solids: Some theoretical principles. *J. Mech. Phys. Solids*, 11:357–372, 1963.

[19] P. V. Houtte. On the equivalence of the relaxed taylor theory and the bishop-hill theory for partially constrained plastic deformation of crystals. *Mater. Sci. Eng*, 55:69–77, 1982.

[20] P. V. Houtte, S. Li, M. Seefeldt, and L. Delannay. Deformation texture prediction: from the taylor model to the advanced lamel model. *Int. J. Plast.*, 21:589–624, 2005.

[21] T. Hui and C. Oskay. Computational modeling of polyurea-coated composites subjected to blast loads. *Journal of Composite Materials*, 46:2167–2178, 2012.

[22] T. Hui and C. Oskay. A high order homogenization model for transient dynamics of heterogeneous media including micro-inertia effects. *Comput. Methods Appl. Mech. Engrg.*, 273:181–203, 2014.

[23] M. Knezevic and D. J. Savage. A high-performance computational framework for fast crystal plasticity simulations. *Comput. Mater. Sci.*, 83:101–106, 2014.

[24] M. Knezevic, S. R. Kalidindi, and D. Fullwood. Computationally efficient database and spectral interpolation for fully plastic taylor-type crystal plasticity calculations of face-centered cubic polycrystals. *Int. J. Plast.*, 24:1264–1276, 2008.

[25] M. Knezevic, R. J. McCabe, R. A. Lebensohn, C. N. Tome, C. Liu, M. L. Lovato, and B. Mihaila. Integration of self-consistent polycrystal plasticity with dislocation density based hardening laws within an implicit finite element framework: Application to low-symmetry metals. *J. Mech. Phys. Solids*, 61:2034–2046, 2013.

[26] V. Kouznetsova, W. A. M. Brekelmans, and F. P. T. Baaijens. An approach to micro-macro modeling of heterogeneous materials. *Comput. Mech.*, 27:37–48, 2001.

[27] R. A. Lebensohn. N-site modeling of a 3d viscoplastic polycrystal using fast fourier transform. *Acta Mater.*, 49:2723–2737, 2001.

[28] R.A. Lebensohn and G.R. Canova. A self-consistent approach for modelling texture development of two-phase polycrystals: Application to titanium alloys. *Acta Mater.*, 45: 3687–3694, 1997.

[29] R.A. Lebensohn and C.N. Tome. A self-consistent anisotropic approach for the simulation of plastic deformation and texture development of polycrystals: Application to zirconium alloys. *Acta Meta. Mater.*, 41:2611–2624, 1993.

[30] R.A. Lebensohn, A.K. Kanjarla, and P. Eisenlohr. An elasto-viscoplastic formulation based on fast fourier transforms for the prediction of micromechanical fields in polycrystalline materials. *Int. J. Plast.*, 32–33:59–69, 2012.

[31] E. B. Marin. On the formulation of a crystal platicity model. Technical report, Sandia National Laboratories, 2006.

[32] J.-C. Michel and P. Suquet. A model-reduction approach to the micromechanical analysis of polycrystalline materials. *Comput. Mech.*, 57:483–508, 2016.

[33] J.C. Michel and P. Suquet. Nonuniform transformation field analysis. *Int. J. Solids Struct.*, 40:6937–6955, 2003.

[34] J.C. Michel and P. Suquet. Computational analysis of nonlinear composite structures using the nonuniform transformation field analysis. *Comput. Methods Appl. Mech. Engrg.*, 193:5477–5502, 2004.

[35] J.C. Michel, H. Moulinec, and P. Suquet. Effective properties of composite materials with periodic microstructure: a computational approach. *Comput. Methods Appl. Mech. engrg.*, 172:109–143, 1999.

[36] C. Miehe, J. Schröder, and J. Schotte. Computational homogenization analysis in finite plasticity simulation of texture development in polycrystalline materials. *Comput. Methods Appl. Mech. Engrg.*, 171:387–418, 1999.

[37] B. Mihaila, M. Knezevic, and A. SCardenas. Three orders of magnitude improved efficiency with high-performance spectral crystal plasticity on gpu platforms. *Int. J. Numer. Methods Eng.*, 83:785–798, 2014.

[38] H. Moulinec and P. Suquet. A numerical method for computing the overall response of nonlinear composites with complex microstructure. *Comput. Methods Appl. Mech. engrg.*, 157:69–94, 1998.

[39] C. Oskay and J. Fish. Eigendeformation-based reduced order homogenization for failure analysis of heterogeneous materials. *Comput. Methods Appl. Mech. Engrg.*, 196:1216–1243, 2007.

[40] T. Ozturk, C. Stein, R. Pokharel, C. Hefferan, H. Tucker, S. Jha, R. John, R. A. Lebensohn, P. Kenesei, R. M. Suter, and A. D. Rollett. Simulation domain size requirements for elastic response of 3d polycrystalline materials. *Modelling Simul. Mater. Sci. Eng.*, 24:015006, 2016.

[41] D. Peirce, R.J. Asaro, and A. Needleman. An analysis of nonuniform and localized deformation in ductile single crystals. *Acta Metall.*, 30:1087–1119, 1982.

[42] C. G. Petra, O. Schenk, and M. Anitescu. Real-time stochastic optimization of complex energy systems on high-performance computers. *IEEE Comput. Sci. Eng.*, 16:32–42, 2014.

[43] C. G. Petra, O. Schenk, M. Lubin, and K. Gärtner. An augmented incomplete factorization approach for computing the schur complement in stochastic optimization. *SIAM J. Sci. Comput.*, 36:C139–C162, 2014.

[44] J.R. Rice. Inelastic constitutive relations for solids: an internal variable theory and its application to metal plasticity. *J. Mech. Phys. Solids*, 19:433–455, 1971.

[45] F. Roters, P. Eisenlohr, T.R. Bieler, and D. Raabe. *Crystal Plasticity Finite Element Methods*. John Wiley and Sons, New York, 1st edition, 2013.

[46] Yousef Saad. *Iterative Methods for Sparse Linear Systems*. Society for Industrial and Applied Mathematics, 2nd edition, 2003.

[47] G. Sachs. Zur ableitung einer fliessbedingung. *Ver. Dtsch. Ing.*, 72:734–736, 1928.

[48] J. Segurado, R. A. Lebensohn, J. LLorca, and C. N. Tome. Multiscale modeling of plasticity based on embedding the viscoplastic self-consistent formulation in implicit finite elements. *Int. J. Plast.*, 28:124–140, 2012.

[49] R.J.M. Smit, W.A.M. Brekelmans, and H.E.H. Meijer. Prediction of the mechanical behavior of nonlinear heterogeneous systems by multi-level finite element modeling. *Comput. Methods Appl. Mech. Engrg.*, 155:181–192, 1998.

[50] D.E. Solas and C.N. Tome. Texture and strain localization prediction using a n-site polycrystal model. *Int. J. Plast.*, 17:737–753, 2001.

[51] G.I. Taylor. Plastic Strain in Metals. *J. Inst. Met.*, 62:307–324, 1938.

[52] J. Thomas, M. Groeber, and S. Ghosh. Image-based crystal plasticity FE framework for microstructure dependent properties of Ti-6Al-4V alloys. *Mater. Sci. Eng. A*, 553: 164–175, 2012.

[53] D. D. Tjahjanto, P. Eisenlohr, and F. Roters. A novel grain cluster-based homogenization scheme. *Modelling Simul. Mater. Sci. Eng.*, 18:015006, 2010.

[54] H. Wang, P.D. Wu, C.N. Tome, and Y. Huang. A finite strain elastic–viscoplastic self-consistent model for polycrystalline materials. *J. Mech. Phys. Solids*, 58:594–612, 2010.

[55] S. Yadegari, S. Turteltaub, and A. Suiker. Generalized grain cluster method for multiscale response of multiphase materials. *Comput. Mech.*, 56:193–219, 2015.

[56] H. Yan, C. Oskay, A. Krishnan, and L. R. Xu. Compression-after-impact response of woven fiber-reinforced composites. *Composites Science and Technology*, 70:2128–2136, 2010.

[57] Z. Yuan and J. Fish. Multiple scale eigendeformation-based reduced order homogenization. *Comput. Methods Appl. Mech. Engrg.*, 198:2016–2038, 2009.

[58] Z. Yuan and J. Fish. Are the cohesive zone models necessary for delamination analysis. *Comput. Methods Appl. Mech. Engrg.*, 310:567–604, 2016.

[59] S. Zhang and C. Oskay. Reduced order variational multiscale enrichment method for elasto-viscoplastic problems. *Comput. Methods Appl. Mech. Engg.*, 300:199–224, 2016.

[60] X. Zhang and C. Oskay. Eigenstrain based reduced order homogenization for polycrystalline materials. *Comput. Methods Appl. Mech. Engrg.*, 297:408–436, 2015.

[61] X. Zhang and C. Oskay. Polycrystal plasticity modeling of nickel-based superalloy in 617 subjected to cyclic loading at high temperature. *Modelling Simul. Mater. Sci. Eng.*, 24: 055009, 2016.